

Title	Surface modification of perfect and hydroxylated TiO <sub>2</sub> rutile (110) and anatase (101) with chromium oxide nanoclusters
Authors	Fronzi, Marco; Nolan, Michael
Publication date	2017-10-17
Original Citation	Fronzi, M. and Nolan, M. (2017) 'Surface Modification of Perfect and Hydroxylated TiO <sub>2</sub> Rutile (110) and Anatase (101) with Chromium Oxide Nanoclusters', ACS Omega, 2(10), pp. 6795-6808. doi: 10.1021/acsomega.7b01118
Type of publication	Article (peer-reviewed)
Link to publisher's version	10.1021/acsomega.7b01118
Rights	© 2017 American Chemical Society. This is an open access article published under an ACS AuthorChoice License, which permits copying and redistribution of the article or any adaptations for non-commercial purposes. - <a href="http://pubs.acs.org/page/policy/authorchoice_termsofuse.html">http://pubs.acs.org/page/policy/authorchoice_termsofuse.html</a>
Download date	2023-05-06 00:39:18
Item downloaded from	<a href="http://hdl.handle.net/10468/4946">http://hdl.handle.net/10468/4946</a>

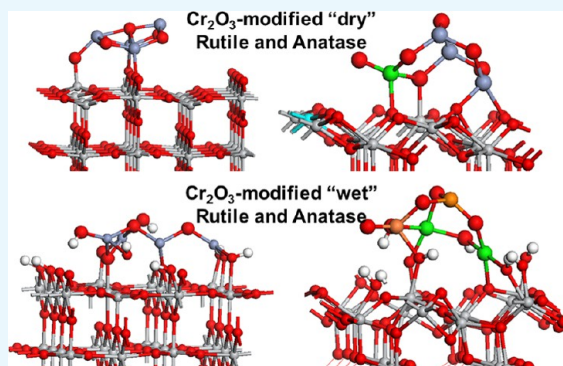
# Surface Modification of Perfect and Hydroxylated TiO<sub>2</sub> Rutile (110) and Anatase (101) with Chromium Oxide Nanoclusters

Marco Fronzi<sup>†</sup> and Michael Nolan<sup>\*†</sup>

Tyndall National Institute, University College Cork, Lee Maltings, Cork T12 RSCP, Ireland

## Supporting Information

**ABSTRACT:** We use first-principles density functional theory calculations to analyze the effect of chromia nanocluster modification on TiO<sub>2</sub> rutile (110) and anatase (101) surfaces, in which both dry/perfect and wet/hydroxylated TiO<sub>2</sub> surfaces are considered. We show that the adsorption of chromia nanoclusters on both surfaces is favorable and results in a reduction of the energy gap due to a valence band upshift. A simple model of the photoexcited state confirms this red shift and shows that photoexcited electrons and holes will localize on the chromia nanocluster. The oxidation states of the cations show that Ti<sup>3+</sup>, Cr<sup>4+</sup>, and Cr<sup>2+</sup> (with no Cr<sup>6+</sup>) can be present. To probe potential reactivity, the energy of oxygen vacancy formation is shown to be significantly reduced compared to that of pure TiO<sub>2</sub> and chromia. Finally, we show that inclusion of water on the TiO<sub>2</sub> surface, to begin inclusion of environment effects, has no notable effect on the energy gap or oxygen vacancy formation. These results help us to understand earlier experimental work on chromia-modified anatase TiO<sub>2</sub> and demonstrate that chromia-modified TiO<sub>2</sub> presents an interesting composite system for photocatalysis.



## 1. INTRODUCTION

Because of growing global energy demands, the depletion of fossil fuel resources, and climate change, the development of efficient materials to convert abundant solar light into chemical fuels is an active research topic. There is significant interest in using photocatalysts in the transformation of solar energy to fuels.<sup>1–3</sup> Of particular importance are the conversion of water into hydrogen and the conversion of the greenhouse gas CO<sub>2</sub> into storable and usable hydrocarbon fuels. The latter can contribute to addressing the problem of climate change by coupling with CO<sub>2</sub> capture to reduce emission of CO<sub>2</sub> into the atmosphere.

Absorption of light by the photocatalyst excites an electron into the conduction band states of the semiconductor photocatalyst.<sup>1–3</sup> The resulting electron and hole charge carriers can migrate through the photocatalyst and reduce or oxidize molecules. This process enables the storage of solar energy into chemical bonds in, for example, hydrogen or liquid fuels, which can be used whenever needed.

The most widely studied material in photocatalysis over the last 40 years is TiO<sub>2</sub>. From a practical perspective, it is cheap, shows good chemical stability, and is earth-abundant. From a fundamental perspective, TiO<sub>2</sub> shows catalytically active surfaces, particularly in anatase, and a relatively high photo-sensitivity.<sup>1–8</sup>

However, there are some issues that have to be addressed to produce highly efficient devices. First, the photoabsorbance of TiO<sub>2</sub> in the visible region of the solar spectrum is still too low for the practical use of solar energy. This is due to the large

band gap of over 3 eV, which lies in the ultraviolet (UV) region of the solar spectrum; UV makes up only 4% of the solar spectrum. The consequence of this is a low efficiency. Second, the lifetime of the separated charge carriers produced after light adsorption is too short and needs to be increased to create electrons and holes that are available for surface reactions over the time scales where catalysis operates.

To address these issues, conventional approaches have exploited the effect of substituting other elements, so-called doping, into the crystal structure of the host photoactive material. For TiO<sub>2</sub>, there has been a significant amount of work on both metal and nonmetal (N, S, and F anions on oxygen sites) doping of TiO<sub>2</sub>.<sup>9–17</sup> This work has primarily focused on band gap reduction to impart a red shift in the absorption edge so that visible light can be absorbed. However, doping of TiO<sub>2</sub> has some issues with respect to stability, reproducibility, and lifetimes, and even today, there are still many issues with doping that are not fully resolved.

Of particular interest for the present work is that chromium doping has been demonstrated to play a role in red shifting light absorption in TiO<sub>2</sub>. Peng et al.<sup>18</sup> showed how the absorption edge of TiO<sub>2</sub> thin films shifts toward longer wavelengths, that is a red shift, from 375 nm in undoped TiO<sub>2</sub> to about 800 nm with increasing Cr concentration. This greatly enhances the absorption of the solar spectrum of TiO<sub>2</sub>

**Received:** August 2, 2017

**Accepted:** September 25, 2017

**Published:** October 17, 2017

nanomaterials.<sup>19,20</sup> However, this doping approach can create defects arising from replacing Ti with another metal or point defects that form to charge-compensate the dopant, and these defects can act as recombination centers, which then reduce the efficiency of the photocatalyst despite an apparent visible light absorption.<sup>18–21</sup>

It has been found that to significantly increase the photoabsorbance, without impacting negatively the catalytic properties, a relatively high doping level should be used, which can then cause a rapid degradation of the crystalline structure.<sup>20</sup> There are thus some significant issues associated with doping of TiO<sub>2</sub>, which need to be addressed if it is to be used as a viable photocatalyst. Some recent alternative approaches have included inducing a high degree of reduction within TiO<sub>2</sub>, by incorporation of hydrogen, the so-called “black TiO<sub>2</sub>”,<sup>22–24</sup> modification with small-band-gap semiconducting quantum dots such as CdS,<sup>25,26</sup> and modification with metal particles to exploit plasmon absorption in metal nanoparticles.<sup>27,28</sup>

A novel and very promising way to address the issues associated with the photoactivity of TiO<sub>2</sub> and doped TiO<sub>2</sub> and improve the efficiency of photocatalytic devices is by nanocluster (NC) modification of TiO<sub>2</sub> surfaces using metal oxide nanoclusters as the modifiers.<sup>29–31</sup> The interaction between the TiO<sub>2</sub> surface and the oxide nanoclusters results in a strong interaction that forms an interface between the surface and adsorbed nanocluster. The new interfacial surface–nanocluster bonds can then modify the atomic and electronic structure of clean TiO<sub>2</sub>. Instead of creating new states in the band gap, which act as recombination centers, a shift in either the valence or conduction band edge is induced, with a consequent reduction of the energy gap between the highest occupied and lowest unoccupied electronic states.<sup>5,32–35</sup> In addition, these surface-modified composite structures can enhance charge separation of electrons and holes with a consequent lengthening of electron–hole lifetimes; this last point has been demonstrated through photoluminescence experiments on surface-modified TiO<sub>2</sub> systems.<sup>34,35</sup> Finally, improved reaction rates for molecular degradation have been observed under illumination in both the visible and UV regions of the solar spectrum.

In an experimental study, Irie et al.<sup>36</sup> used impregnation synthesis to prepare anatase TiO<sub>2</sub> modified with Cr<sub>2</sub>O<sub>3</sub> by grafting Cr<sup>3+</sup> ions and forming supported amorphous Cr<sub>2</sub>O<sub>3</sub> structures. This composite structure showed promising results for band gap reduction and charge separation, together with high chemical stability and greatly enhanced performance over Cr-doped anatase. Photocatalytic activity was evaluated by 2-propanol decomposition under visible light (1 mW cm<sup>−1</sup>, between 450 and 580 nm), and this was improved over the Cr-doped TiO<sub>2</sub> system. These findings were attributed to a reduction in charge recombination in the chromia-grafted system. Although a direct observation of electron transfer from Cr<sub>2</sub>O<sub>3</sub> to TiO<sub>2</sub> upon excitation was not directly shown, it was assumed to be the process involved. Such information is crucial to determining the catalytic activity of the surface and is therefore a fundamental objective of our analysis.

This article thus presents a first-principles analysis of the properties of Cr<sub>2</sub>O<sub>3</sub>-nanocluster-modified rutile and anatase TiO<sub>2</sub> surfaces using density functional theory (DFT) corrected for on-site Coulomb interactions (DFT + *U*), to gain insights into the fundamental properties of the resulting composite system. We consider first sub-nanometer, or low coverage of, chromia nanoclusters of composition Cr<sub>2</sub>O<sub>3</sub> and Cr<sub>4</sub>O<sub>6</sub>

adsorbed on rutile (110) and anatase (101) surfaces; these are the most stable low-index surfaces of each form of TiO<sub>2</sub>. Furthermore, we also investigate the modification of “wet” TiO<sub>2</sub> surfaces, that is, surfaces that have been hydroxylated by dissociation of water. The size of the nanocluster has been chosen based on arguments in previous studies from our group,<sup>29–31,37–39</sup> and these can be considered as representatives of molecular-sized chromia nanoclusters. In considering a practical photocatalyst, it is not enough to have only light absorption in the visible region and one needs to consider charge separation and the nature of the TiO<sub>2</sub> support, whether it be “dry/perfect” or “wet/with surface hydroxyls” before surface modification with the nanoclusters. This allows us to move toward, at least in part, more realistic catalytic conditions. Water on TiO<sub>2</sub> surfaces has been well-studied<sup>40–46</sup> and at moderate coverages, such as 1/2 a monolayer (ML), can show a mixture of hydroxyl groups and molecular water. Charge separation is treated in a model of the photoexcited state to examine where electrons and holes are likely to localize after photoexcitation,<sup>47–52</sup> and this is crucial in studying possible recombination issues.

The final aspect addressed is the formation of oxygen vacancies because TiO<sub>2</sub> and Cr<sub>2</sub>O<sub>3</sub> are reducible and earlier work from our group<sup>53,54</sup> suggests that O vacancies can form with a low energy cost in the supported nanoclusters. In addition, these defects represent potential sites for adsorption of molecules and may be catalytically active and are thus of importance for the properties of these composite materials.

The results in this article show that the modification of rutile and anatase TiO<sub>2</sub> surfaces with small chromia nanoclusters can induce a red shift in light absorption, irrespective of the nature of the TiO<sub>2</sub> surface, that is whether dry or modified with water. The reactivity is also enhanced over both TiO<sub>2</sub> and Cr<sub>2</sub>O<sub>3</sub>, as measured by the high reducibility of the composite structures. Formation of Cr<sup>6+</sup> species is not predicted. Chromia-modified TiO<sub>2</sub> composites are thus proposed as potential visible light-activated photocatalysts.

## 2. RESULTS

**2.1. Cr<sub>2</sub>O<sub>3</sub> Nanocluster Modification of Dry TiO<sub>2</sub> Rutile (110) and Anatase (101) Surfaces.** In this section, we analyze the properties of Cr<sub>2</sub>O<sub>3</sub> nanocluster (NC)-modified rutile (110) and anatase (101) surfaces, in which no water or point defects are present. The geometry of each composite system has been determined by structural optimization of two representative noncrystalline Cr<sub>2</sub>O<sub>3</sub>-nanoclusters, with Cr<sub>2</sub>O<sub>3</sub> and Cr<sub>4</sub>O<sub>6</sub> stoichiometries,<sup>36</sup> which have been relaxed in the gas phase within the computational setup described in Section 2. These nanoclusters are adsorbed on the rutile (110) and anatase (101) surfaces in different configurations (see Figure S1, Supporting Information, for other higher-energy structural isomers that we found; on the basis of our earlier work,<sup>51,53,55</sup> we expect that there to be little significant effect of the precise structure on the properties of these composite systems), and the composite nanocluster–TiO<sub>2</sub> structures are relaxed with no symmetry constraints. We calculate the nanocluster adsorption energies on the TiO<sub>2</sub> surfaces, relative to a free nanocluster and a bare surface, as follows

$$E^{\text{ads}} = E^{\text{Cr}_2\text{O}_3\text{--TiO}_2} - [E^{\text{TiO}_2} + E^{\text{Cr}_2\text{O}_3}]$$

where  $E^{\text{Cr}_2\text{O}_3\text{--TiO}_2}$ ,  $E^{\text{TiO}_2}$ , and  $E^{\text{Cr}_2\text{O}_3}$  are the computed total energies of the nanocluster-modified TiO<sub>2</sub> composite, the



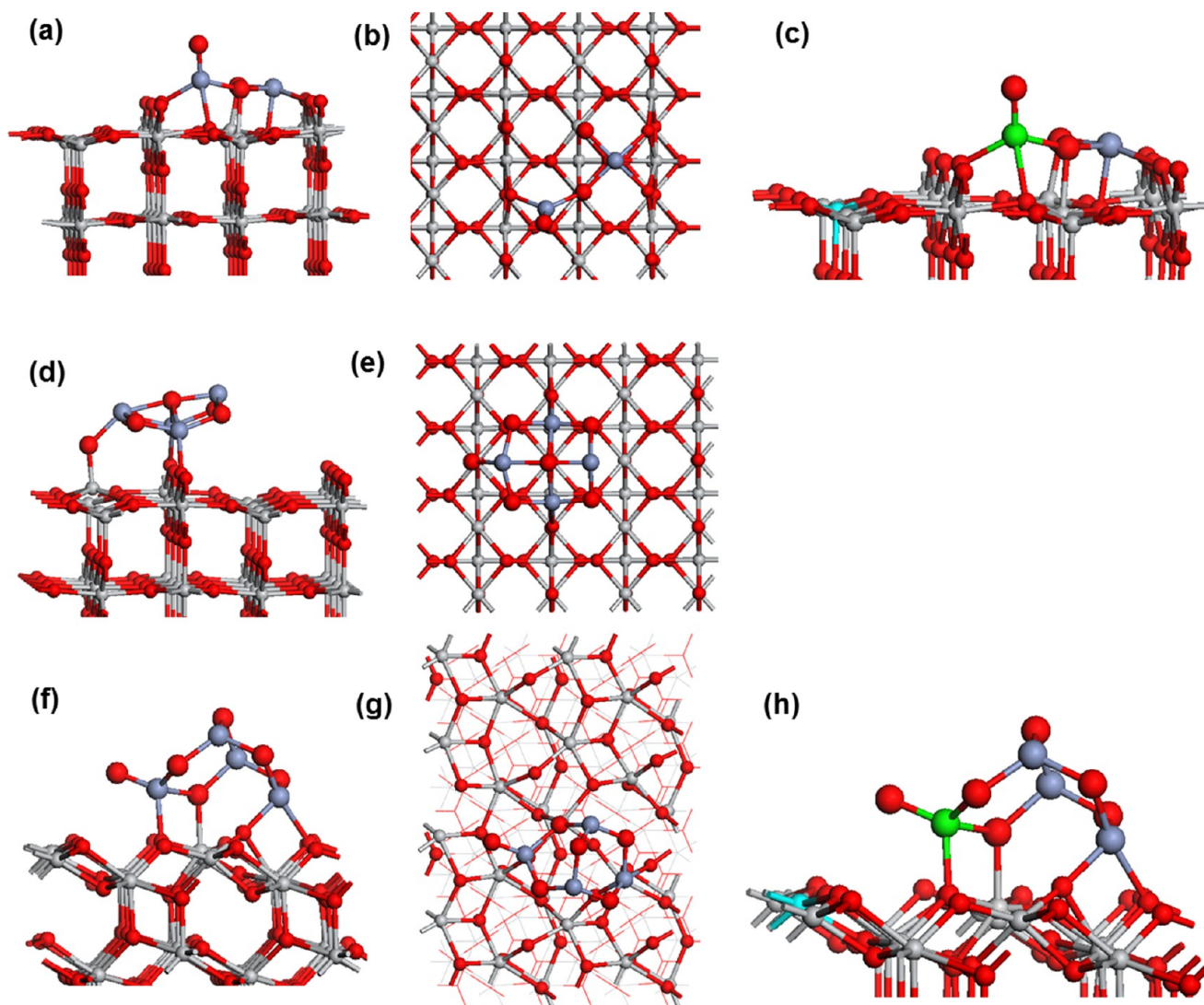


**Figure 1.** Atomic structure of  $\text{Cr}_2\text{O}_3$  and  $\text{Cr}_4\text{O}_6$  nanoclusters adsorbed on the  $\text{TiO}_2$  rutile (110) and  $\text{TiO}_2$  anatase (101) surfaces. The left panels show a side view, the middle panels show a plan view, and the right panels show the location of reduced  $\text{Ti}^{3+}$  and oxidized  $\text{Cr}^{4+}$  species, which are cyan and green, respectively. Structures in panels (a)–(c) represent stoichiometric  $\text{Cr}_2\text{O}_3$  adsorbed on rutile (110). Structures in panels (d) and (e) represent stoichiometric  $\text{Cr}_4\text{O}_6$  adsorbed on rutile (110). Panels (f)–(h) represent stoichiometric  $\text{Cr}_4\text{O}_6$  adsorbed on anatase (101). In this and all subsequent figures, the red spheres represent oxygen atoms, blue-gray spheres represent  $\text{Ti}^{4+}$ , cyan spheres represent  $\text{Ti}^{3+}$ , dark blue spheres represent  $\text{Cr}^{3+}$  atoms, and green spheres represent  $\text{Cr}^{4+}$  atoms.

unmodified bare  $\text{TiO}_2$  surface, and the free, stoichiometric chromia nanoclusters, respectively. In the most stable adsorption configuration, the computed adsorption energy of  $\text{Cr}_2\text{O}_3$  on rutile (110) is  $E^{\text{ads}} = -6.24$  eV. For the  $\text{Cr}_4\text{O}_6$  nanocluster, the computed adsorption energies are  $E^{\text{ads}} = -4.24$  eV on rutile (110) and  $E^{\text{ads}} = -5.85$  eV on anatase (101). The adsorption energies show a strong interaction between the surface and the chromia nanoclusters, and, as discussed in the previous work,<sup>55</sup> these energies indicate that the nanocluster will remain bound to the surface and will not aggregate into larger structures that could reduce the effect of the surface modification.

After nanocluster adsorption and structural relaxation, we observe the formation of new interfacial Cr–O and Ti–O bonds between the surface and the nanoclusters. Figure 1 shows the atomic structure of chromia nanocluster-modified rutile (110) and anatase (101), whereas Figure S2 in the Supporting Information shows the key interatomic distances, which we now briefly discuss and which are discussed in detail

in the Supporting Information. In  $\text{Cr}_2\text{O}_3$ –rutile (110), the Cr cations are 4-fold-coordinated and bind to in-plane and bridging surface oxygens in rutile (110). The 3-fold-coordinated oxygens in the nanocluster bind to 5-fold-coordinated surface Ti atoms, with Ti–O distances of 1.78 and 2.02 Å, and these Ti atoms migrate away from the surface plane toward the nanocluster by up to 0.5 Å. The third oxygen forms a chromyl  $\text{Cr}=\text{O}$  species, with a typical short Cr–O distance of 1.60 Å. This is different to, for example,  $\text{Fe}_2\text{O}_3$ –modified rutile (110) from our earlier work,<sup>56</sup> and if we use the most stable  $\text{Fe}_2\text{O}_3$ –rutile structure as input, this is less stable after relaxation than the structure shown in Figure 1a.

In  $\text{Cr}_4\text{O}_6$ –modified rutile (110), the two 4-fold-coordinated Cr cations bind to bridging oxygen atoms in rutile (110) with Cr–O distances of 1.82 and 2.02 Å. The other 3-fold-coordinated Cr atoms do not bind to the surface. Lower coordinated Cr atoms have generally shorter Cr–O distances, which is typical for structures with low coordinated metal cations. There is one Ti–O bond between a 5-fold-coordinated

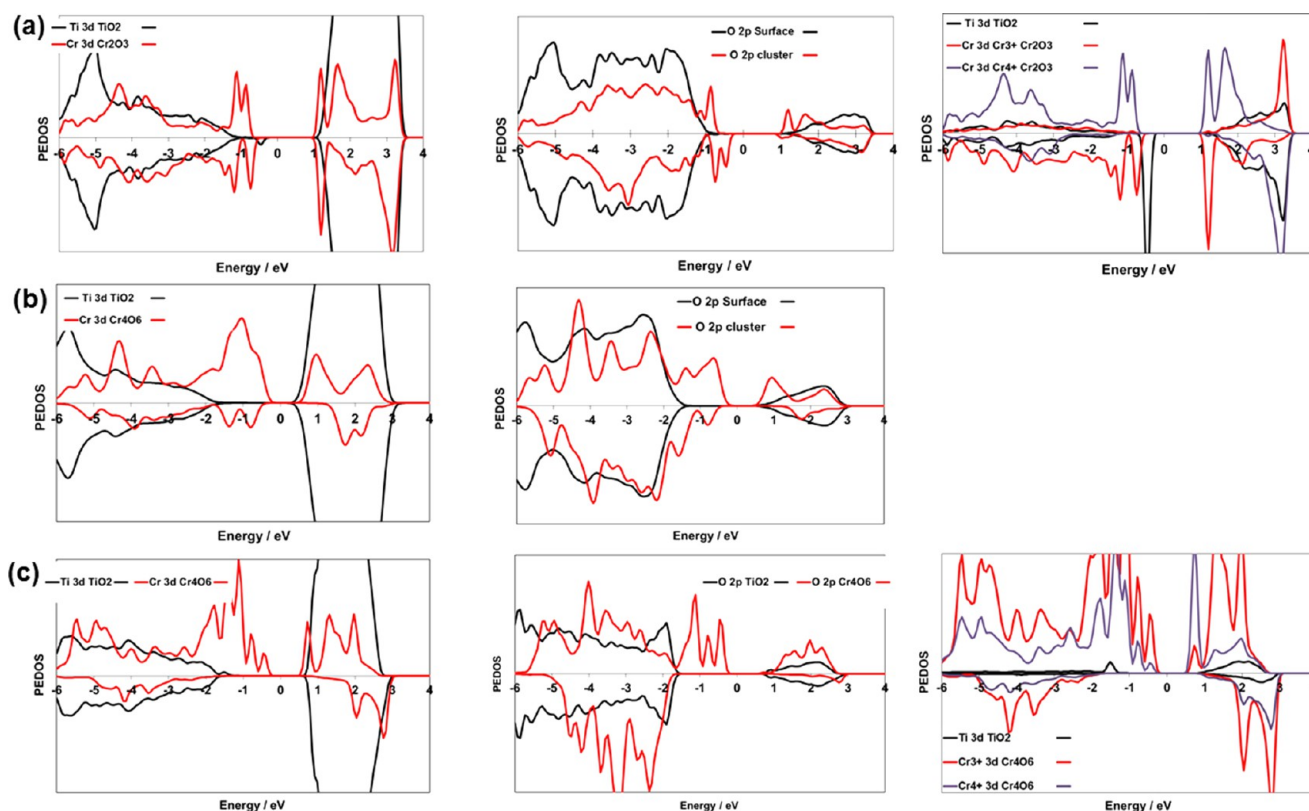


**Figure 2.** Projected electronic density of states (PEDOSs) projected onto the Ti 3d and Cr 3d states in the  $\text{Cr}_2\text{O}_3$ – $\text{TiO}_2$  composites (left column), the O 2p states of the adsorbed chromia nanoclusters and  $\text{TiO}_2$  surfaces (middle column), and the  $\text{Ti}^{3+}$  and  $\text{Cr}^{4+}$  states for Ti and Cr cations (right column). (a)  $\text{Cr}_2\text{O}_3$ -modified rutile (110), (b)  $\text{Cr}_4\text{O}_6$ -modified rutile (110), and (c)  $\text{Cr}_4\text{O}_6$ -modified anatase (101). The zero of energy is the Fermi level.

surface Ti atom and a 2-fold-coordinated nanocluster oxygen (Ti–O distance = 1.78 Å), and this Ti atom migrates out of the surface layer by 0.5 Å.

In the  $\text{Cr}_4\text{O}_6$ –anatase composite, two Cr cations bind to the oxygen in the anatase surface. One Cr cation is 4-fold-coordinated and binds to a surface oxygen with a Cr–O distance of 1.89 Å. The 4-coordinate Cr atom bridges two surface oxygen atoms with Cr–O distances of 1.95 and 2.08 Å. There is one Ti–O bond between the surface and the nanocluster, with a Ti–O distance of 2.02 Å. Within the nanocluster, there is a chromyl bond, to a 4-coordinate Cr cation, with a Cr–O distance of 1.65 Å.

We observe that the more nanoclusters–surface bonds that are formed the higher the stability of the adsorbed chromia nanocluster, for example, the  $\text{Cr}_4\text{O}_6$ –rutile system has the fewest interfacial bonds and the lowest nanocluster adsorption energy.

Figure 2 shows the computed projected electronic density of states (PEDOSs) projected onto the Ti 3d and Cr 3d states of the chromia composites, the O 2p states of oxygen in the chromia nanoclusters, and the  $\text{TiO}_2$  surface. We also show the PEDOS of those Ti and Cr atoms with oxidation states other than +4 and +3.

In all chromia– $\text{TiO}_2$  composites, we find a strong change around the valence-to-conduction band energy gaps when compared to those in the unmodified rutile and anatase surfaces. If we consider first the overall features of the PEDOS, we see that there are new occupied electronic states derived from both Cr 3d and O 2p present above the original valence band edge of both  $\text{TiO}_2$  surfaces. Thus, the modification of

rutile and anatase with chromia nanoclusters results in an upshift of the energy of the highest-lying occupied electronic states relative to that of unmodified  $\text{TiO}_2$ . The composition of these highest-energy occupied states is consistent with the character of bulk  $\text{Cr}_2\text{O}_3$  in which the valence band edge is composed of both Cr 3d and O 2p states.

The upshift within our DFT + *U* computational scheme is as large as 1.5 eV for rutile and 1.8 eV for modified anatase. These shifts are clearly quantitatively dependent on the DFT functional used (generalized gradient approximation (GGA), GGA + *U*, or hybrid DFT); the key point is that the chromia modification, which introduces new interfacial bonds, shifts the position of the highest occupied electronic states to higher energy. Thus, the energy gap is reduced and absorption of light is shifted to longer wavelengths, allowing for visible light absorption.

On examining the nature of the conduction band edge, we see that the  $\text{TiO}_2$  and chromia states are essentially isoenergetic so that it is the modification of electronic states around the valence band edge that produces the red shift in light absorption in chromia-modified  $\text{TiO}_2$ . This is consistent with and explains the results of Irie et al.<sup>36</sup>

A closer examination of the Ti 3d PEDOS of the  $\text{Cr}_2\text{O}_3$ –rutile and  $\text{Cr}_4\text{O}_6$ –anatase systems shows the appearance of a Ti 3d-derived electronic state that lies inside the original rutile  $\text{TiO}_2$  valence-to-conduction band energy gap, at ca. 0.8 eV above the rutile valence band edge and 0.1 eV above the anatase valence band edge. This in-gap electronic state is typical of a reduced  $\text{Ti}^{3+}$  species in the surface.<sup>57,58</sup> There is no  $\text{Ti}^{3+}$  state present in  $\text{Cr}_4\text{O}_6$ –rutile.

To examine in detail the oxidation states of Ti, Cr, and O in the nanocluster and the  $\text{TiO}_2$  surfaces, we have computed the Bader charges and spin magnetizables on all atoms. For the  $\text{Cr}_2\text{O}_3$ –rutile system, there is a surface 5-fold-coordinated Ti cation (indicated in Figure 1c) that has a computed Bader charge of 1.70 electrons and a spin magnetization of  $0.94 \mu_B$ ; for comparison, oxidized  $\text{Ti}^{4+}$  cations in these systems have computed Bader charges of 1.3 electrons and zero spin magnetization. The local geometry around this Ti site shows elongated Ti–O distances of 2.03–2.08 Å, typical of a localized  $\text{Ti}^{3+}$  site; this compares to 1.90–1.98 Å for the remaining  $\text{Ti}^{4+}$  atoms. The in-gap electronic state, the Bader charge, and spin magnetization for this surface Ti atom are consistent with the formation of a reduced  $\text{Ti}^{3+}$  species. We tested starting structures where this Ti was oxidized, but after relaxation, this reduced species is found.

In the nanocluster, the Cr cations have computed Bader charges of 9.9 and 10.1 electrons, with corresponding computed spin magnetizables of 2.20 and  $2.9 \mu_B$ . With a computed Bader charge of 10.4 electrons and a spin magnetization of  $3 \mu_B$  for  $\text{Cr}^{3+}$  in bulk  $\text{Cr}_2\text{O}_3$ , these results suggest the presence of one  $\text{Cr}^{3+}$  species and an oxidized  $\text{Cr}^{4+}$  species. This then indicates the transfer of one electron from the nanocluster to the rutile (110) surface.

In the  $\text{Cr}_4\text{O}_6$ –rutile structure, there is no Ti 3d state in the  $\text{TiO}_2$  band gap. The computed Bader charges and spin magnetizables for Ti cations in the rutile (110) surface are +1.3 electrons and  $0.0 \mu_B$ , respectively, which are consistent with  $\text{Ti}^{4+}$  species. The computed Bader charges and spin magnetizations on Cr species in the nanocluster are 10.3, 10.3, 10.4, and 10.3 electrons and  $3 \mu_B$  (on all Cr), respectively. These are consistent with the expected  $\text{Cr}^{3+}$  oxidation state in a nanocluster of this stoichiometry.

In  $\text{Cr}_4\text{O}_6$ –anatase, the new Ti 3d-derived state lies less deep in the energy gap than the  $\text{Ti}^{3+}$  state in the rutile (110) surface. The computed Bader charge is 1.70 electrons, the spin magnetization is  $0.96 \mu_B$ , and the local geometry around this Ti site shows elongated Ti–O distances of 2.02 to 2.15 Å. Taken together, these results confirm the presence of a  $\text{Ti}^{3+}$  cation in the surface, the position of which is shown in Figure 1h. In the nanocluster, the Cr cations have computed Bader charges of 10.4, 10.4, 10.3, and 10.1 electrons, with the corresponding computed spin magnetizables being 3, 3, 3, and  $2.1 \mu_B$ . This thus indicates the presence of three  $\text{Cr}^{3+}$  species and a single  $\text{Cr}^{4+}$  species, which is consistent with transfer of an electron from the nanocluster to the anatase (101) surface. The location of the  $\text{Cr}^{4+}$  species is shown in Figure 1h.

**2.2. Nature of the Photoexcited State in  $\text{Cr}_4\text{O}_6$  Nanocluster-Modified Dry  $\text{TiO}_2$  Rutile (110) and Anatase (101) Surfaces.** To study the localization of photoexcited electrons and holes in chromia-modified  $\text{TiO}_2$ , we use a model system in which a triplet electronic state is imposed. The utility of this model in understanding electron and hole localization in anatase bulk and (101),<sup>47</sup> in hole localization in  $\text{ZrO}_2$ ,<sup>50</sup> and in our own work on surface-modified  $\text{TiO}_2$ <sup>30,31,51,52</sup> has been well-explored. Enforcing a triplet spin configuration means that one electron occupies a previously empty conduction band state and a hole is present in the valence band, thus allowing the system to model a photoexcited electronic state. As discussed in Section 4 on Calculation Methods, there are three quantities that we calculate: the vertical, relaxed singlet–triplet, and the relaxation energies. These are denoted  $E^{\text{vertical}}$ ,  $E^{\text{S–T}}$ , and  $E^{\text{relax}}$ , and the energies are presented in Table 1.

**Table 1. Computed Vertical Singlet–Triplet Energy Difference,  $E^{\text{vertical}}$ ; Relaxed Singlet–Triplet Energy Difference,  $E^{\text{S–T}}$ ; and the Relaxation Energy,  $E^{\text{relax}}$ , in  $\text{Cr}_4\text{O}_6$  Nanocluster-Modified  $\text{TiO}_2$  Anatase (101) and Rutile (110)<sup>a</sup>**

structure	$E^{\text{vertical}}$ /eV	$E^{\text{S–T}}$ /eV	$E^{\text{relax}}$ /eV
rutile (110)	2.21	1.69	0.52
anatase (101)	2.27	1.90	0.37
$\text{Cr}_4\text{O}_6$ –rutile (110)	2.14	1.30	0.84
$\text{Cr}_4\text{O}_6$ –anatase (101)	1.55	0.44	1.11

<sup>a</sup>The energies for the bare surfaces are included for comparison.

The vertical energy,  $E^{\text{vertical}}$ , that we have obtained for the modified surfaces is similar to the valence band conduction band energy difference extracted from analysis of the PEDOS. For chromia-modified  $\text{TiO}_2$ , this value is smaller when compared to that for the bare  $\text{TiO}_2$  surfaces, further confirming the reduction in the energy gap after adsorption of the nanocluster.

The singlet–triplet energy difference,  $E^{\text{S–T}}$ , includes the effect of relaxing the geometry after promoting an electron to the conduction band; this value is always smaller than the vertical singlet–triplet energy. This calculation allows us to probe the localization of excited electrons and holes. On both  $\text{TiO}_2$  surfaces, the effect of the  $\text{Cr}_4\text{O}_6$  nanocluster modification is a decrease in the singlet–triplet energy difference by 0.4 and 1.46 eV when compared to that for the corresponding unmodified rutile (110) and anatase (101) surfaces. Thus, we conclude that chromia modifications of  $\text{TiO}_2$  can induce a significant red shift of light absorption in rutile or anatase, which is consistent with experimental work.<sup>36</sup>

The final energy is the relaxation energy,  $E^{\text{relax}}$ , which is an indicator of electron and hole stability after excitation. On  $\text{Cr}_4\text{O}_6$ –rutile and  $\text{Cr}_4\text{O}_6$ –anatase, the relaxation energies are 0.84 and 1.11 eV, respectively. Compared to those of the unmodified surfaces, these energies suggest an enhanced trapping and stabilization of photoexcited electrons and holes after chromia nanocluster modification of  $\text{TiO}_2$ . This may help us to reduce charge recombination in these composite systems.

Figure 3 shows the atomic structure and location of the electron and hole sites in the relaxed triplet electronic configuration for  $\text{Cr}_4\text{O}_6$ –rutile (110) and  $\text{Cr}_4\text{O}_6$ –anatase (101). In the  $\text{Cr}_4\text{O}_6$ –rutile system, the computed Bader charge of 10.5 electrons and the spin magnetization of  $3.5 \mu_B$  show that a  $\text{Cr}^{2+}$  species forms after electron localization on the  $\text{Cr}_4\text{O}_6$  nanocluster. The hole is found on a nanocluster oxygen atom (shown in yellow in Figure 3a) with a computed Bader charge of 6.6 electrons and a spin magnetization of  $0.7 \mu_B$  that are typical of an oxygen hole species.<sup>59,60</sup> The local geometry around the 4-fold-coordinated  $\text{Cr}^{2+}$  site shows Cr–O distances of 1.92–2.11 Å. Around the oxygen hole, the Cr–O distances are 1.78 and 1.91 Å.

In  $\text{Cr}_4\text{O}_6$ –anatase, the computed Bader charges and spin magnetizables on Cr are 10.39, 10.38, 10.3, and 10 electrons and 3.5, 3, 3, and  $2 \mu_B$ , respectively. This indicates that the Cr cations have not changed oxidation states upon excitation. The computed Bader charges for Ti show that two reduced  $\text{Ti}^{3+}$  species are produced after excitation, as indicated with the cyan spheres in Figure 3. The  $\text{Ti}^{3+}$  sites have computed Bader charges and spin magnetizables of 1.71 and 1.72 electrons and 0.80 and  $0.95 \mu_B$ , respectively. The hole localizes on the chromyl oxygen in the nanocluster with a computed Bader charge of 6.81 electrons and a spin magnetization of  $0.75 \mu_B$ .



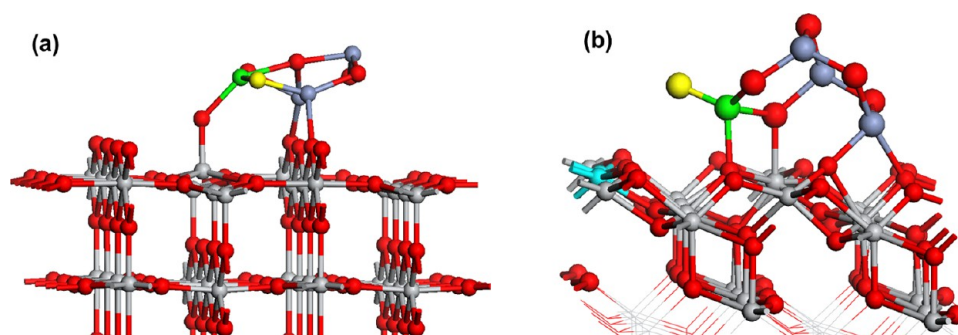


**Figure 3.** Atomic structure and charge localization sites in the triplet state of  $\text{Cr}_4\text{O}_6$ -modified (a) rutile and (b) anatase.  $\text{Cr}^{2+}$  sites are orange,  $\text{Cr}^{4+}$  sites are green,  $\text{O}^-$  sites are yellow, and  $\text{Ti}^{3+}$  sites are cyan.

**Table 2.** Computed Oxygen Vacancy Formation Energies in the  $\text{Cr}_4\text{O}_6$  Nanocluster-Modified Rutile (110) and Anatase (101)  $\text{TiO}_2$  Surfaces

O vacancy site	$\text{Cr}_4\text{O}_6$ -rutile (110)	O vacancy formation energy/eV	O vacancy site	$\text{Cr}_4\text{O}_6$ -anatase (101)	O vacancy formation energy/eV
I		5.03	I		4.77
II		6.2	II		4.06
III		0.22	III		1.95
IV		4.11	IV		2.03
V		3.27	V		3.25
VI		6.29	VI		2.05

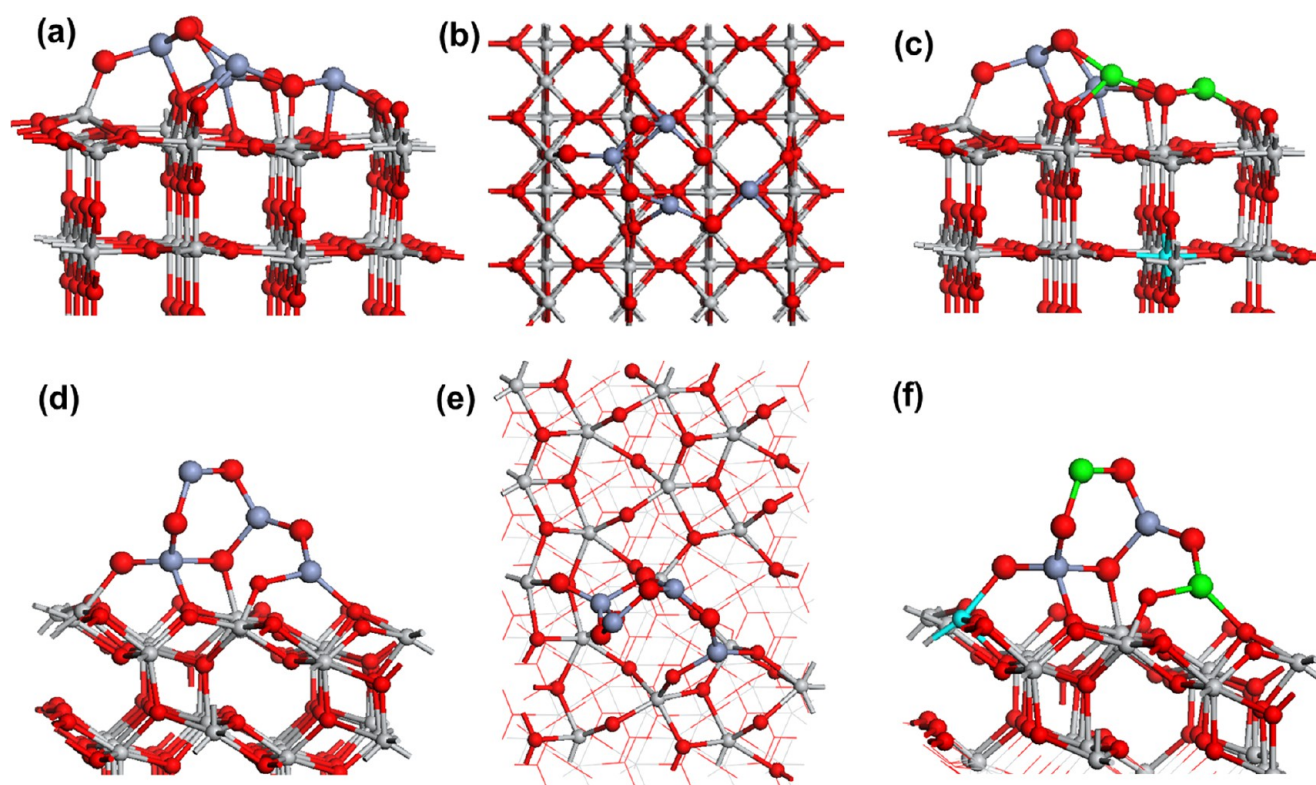


**Figure 4.** Atomic structure of  $\text{Cr}_4\text{O}_6$  nanoclusters adsorbed on the  $\text{TiO}_2$  rutile (110) and  $\text{TiO}_2$  anatase (101) surfaces after formation of the most stable oxygen vacancy in the nanocluster. The left panels show a side view, the middle panels show a plan view, and the right panels show the location of reduced  $\text{Ti}^{3+}$  and  $\text{Cr}^{2+}$  species, which are cyan and green, respectively. Structures representing (a–c)  $\text{Cr}_4\text{O}_6$  adsorbed on rutile (110) and (d–f)  $\text{Cr}_4\text{O}_6$  adsorbed on anatase (101).

The  $\text{Cr}-\text{O}^-$  distance is 1.62 Å, which is a typical distance for a cation–oxygen hole bond. Thus, upon excitation, the valence band hole and conduction band electron can localize on the chromia nanocluster modifier and anatase  $\text{TiO}_2$  surface. The electron transfer proposed by Irie et al. in chromia-modified

anatase may therefore arise from the localization of excited electrons on the  $\text{TiO}_2$  surface. However, we note that for this particular composite system the electron and hole are in close proximity, which is in contrast to other modified  $\text{TiO}_2$  systems we have studied.<sup>31,38,39,51</sup> Thus, electron and hole recombina-

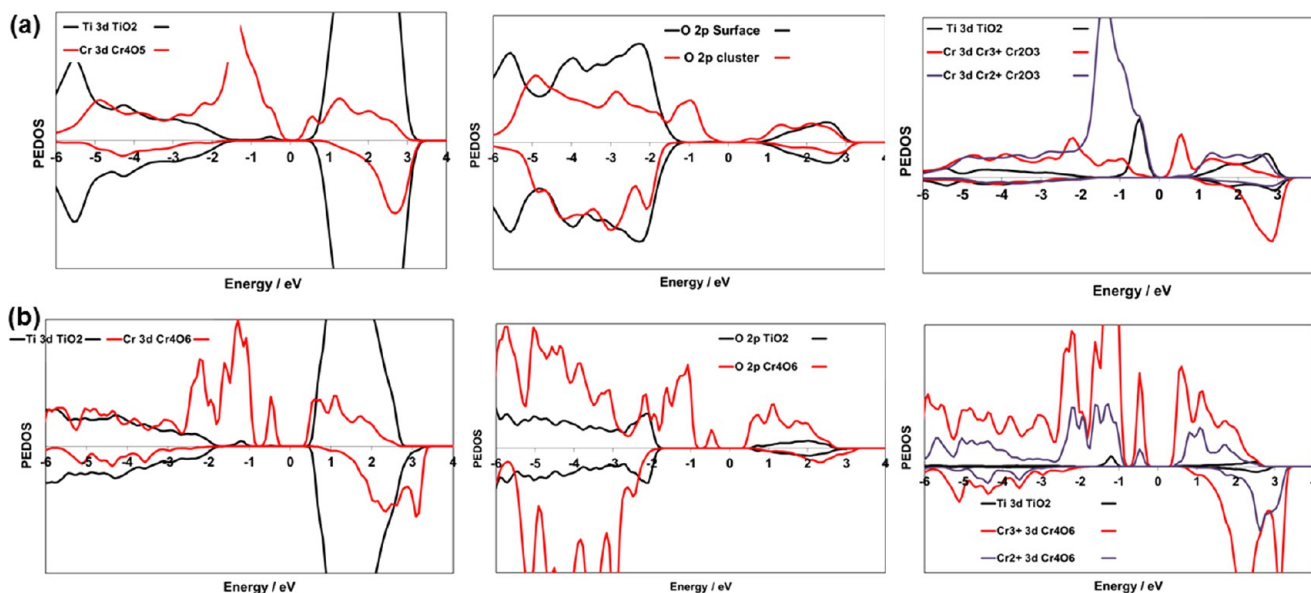


**Figure 5.** Projected electronic density of states (PEDOSs) projected onto the Ti 3d and Cr 3d states in the  $\text{Cr}_2\text{O}_3$ – $\text{TiO}_2$  composites with an oxygen vacancy (left column), the O 2p states of the adsorbed chromia nanoclusters and  $\text{TiO}_2$  surfaces (middle column), and the Ti 3d and Cr 3d states for Ti and Cr species with oxidation states other than  $\text{Ti}^{4+}$  and  $\text{Cr}^{3+}$  (right column). (a)  $\text{Cr}_4\text{O}_6$ -modified rutile (110) and (b)  $\text{Cr}_4\text{O}_6$ -modified anatase (101). The zero of energy is the Fermi level.

tion could readily take place with a consequent impact on the photocatalytic activity of the chromia– $\text{TiO}_2$  composite system. On the other hand, the large relaxation (trapping) energies of the electron–hole pair may mitigate against this. We propose that the ideal electronic structure of these composites would show valence and conduction band edge characters that promote electron and hole separation rather than both being composed of states from the nanocluster or the surface.

**2.3. Oxygen Vacancy Formation in  $\text{Cr}_4\text{O}_6$  Nanocluster Modification of Dry  $\text{TiO}_2$  Rutile (110) and Anatase (101) Surfaces.** Oxygen vacancy formation energies were computed for each oxygen in the adsorbed chromia nanoclusters, and the formation energies are shown in Table 2; Figure S3 in the Supporting Information shows the numbering scheme for the oxygen vacancies. For  $\text{Cr}_4\text{O}_6$ –rutile, we found a very low energy, stable oxygen vacancy site (number III) with a computed formation energy of 0.22 eV, whereas all other sites have formation energies larger than 3 eV. This energy indicates that vacancies can form at low temperatures, but the magnitude of the energy could suggest that these may not be so reactive as the vacancy healing process may be difficult. For  $\text{Cr}_4\text{O}_6$ –anatase, the most stable oxygen vacancy has a computed formation energy of 1.95 eV, which would be a significant reduction over unmodified anatase and bulk  $\text{Cr}_2\text{O}_3$  and is large enough that this vacancy will not be overstabilized and can act as an active site for adsorption of molecules such as  $\text{CO}_2$ . We have also calculated the energy to form the second oxygen vacancy, and we obtain formation energy of 5.86 eV for  $\text{Cr}_4\text{O}_6$ –rutile for vacancy site V.

After vacancy formation in  $\text{Cr}_4\text{O}_6$ –rutile, there is a substantial change in the atomic structure of the adsorbed chromia nanocluster, shown in Figure 4. The key cation–oxygen distances are shown in Figure S4, Supporting Information, and the structural features are discussed in detail in the Supporting Information. Briefly, new bonds form between three Cr atoms in the nanocluster and the surface oxygen (Cr–O distances are 1.96, 1.98, 2.10, and 2.14 Å). New

bonds form between the surface Ti and nanocluster oxygen with these Ti migrating by 0.3–0.9 Å out of the surface layer. The formation of the vacancy facilitates a very strong distortion to the nanocluster structure in which Cr and O that were not bound to the surface now migrate toward the surface to form new interfacial bonds. This is likely the origin of the low vacancy formation energy, the cost to remove oxygen is compensated by the gain in energy when new nanocluster-to-surface bonds are formed.

In the most stable oxygen vacancy structure for  $\text{Cr}_4\text{O}_6$ –anatase, the original chromyl oxygen binds with a surface Ti atom (Ti–O distance of 2.08 Å). Another oxygen in the nanocluster binds to surface Ti with a Ti–O distance of 2.03 Å, and two Cr cations bind to the surface oxygen with Cr–O distances of 1.85 and 1.96/1.99 Å, respectively. Cr–O bonds in the nanocluster generally contract after the vacancy formation, reflecting the reduced coordination of Cr in the nanocluster.

The PEDOS plots are shown in Figure 5 for the most stable oxygen vacancy structure in  $\text{Cr}_4\text{O}_6$ -modified rutile and anatase. In both structures, the general features of the PEDOS are very similar. There are nanocluster-derived electronic states lying above the valence band edge of the  $\text{TiO}_2$  surfaces, and there are localized Cr 3d-derived peaks that lie in the gap between the main Cr valence band peak and the empty conduction band states.

In defective  $\text{Cr}_4\text{O}_6$ –rutile, a Ti 3d-derived gap state is present. This  $\text{Ti}^{3+}$  species has a computed Bader charge of 1.67 electrons and a spin magnetization of 0.9  $\mu_B$ , with Ti–O distances elongated by 0.2 Å compared to the corresponding  $\text{Ti}^{4+}$ –O distances. On Cr, the computed Bader charges and spin magnetizables are 10.1, 10.2, 10.5, and 10.5 electrons, and 3, 3, 3.7, and 3.7  $\mu_B$ , respectively. Thus, the two electrons released by the oxygen vacancy localize onto one subsurface  $\text{Ti}^{3+}$  site (typical for the  $\text{Ti}^{3+}$  species in rutile (110)<sup>61,62</sup>), and the second electron spreads over two Cr sites (with the larger computed Bader charges, green spheres in Figure 4) in the



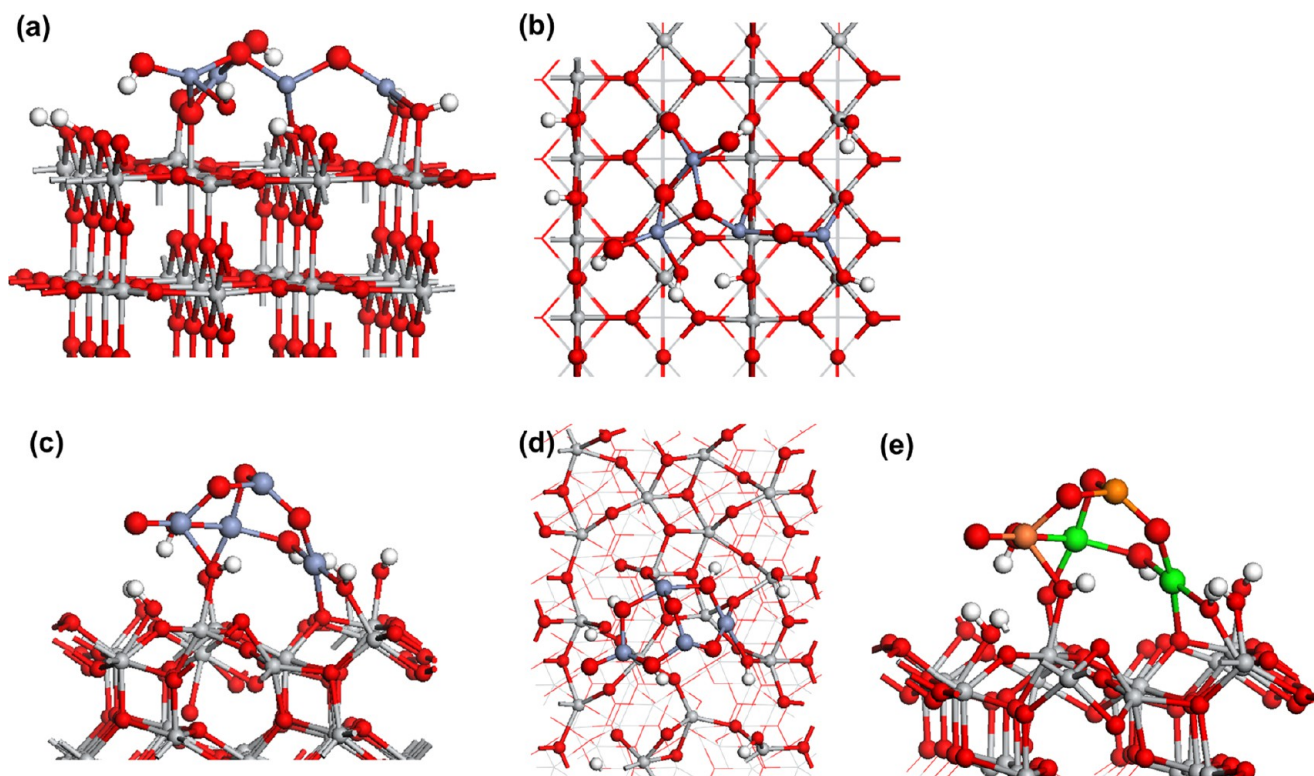


**Figure 6.** Relaxed atomic structure of the  $\text{Cr}_4\text{O}_6$  nanocluster adsorbed on (a, b) rutile (110) and (c–e) anatase (101), with 1/2 ML water coverage on each  $\text{TiO}_2$  surface. The left panels show a side view, the middle panels show a top view, and the right panels show the locations of  $\text{Cr}^{4+}$  and  $\text{Cr}^{2+}$  cations, which are orange and green, respectively.

$\text{Cr}_4\text{O}_6$  nanocluster. The different  $\text{Cr}^{3+}$  and  $\text{Cr}^{2+}$  PEDOS peaks are apparent in Figure 5.

In the defective  $\text{Cr}_4\text{O}_6$ –anatase (101) composite, the Cr atoms have computed Bader charges and spin magnetizables of 10.42, 10.8, 10.6, and 10.2 electrons and 3, 3.6, 3.5, and  $2.1 \mu_B$ , respectively. The  $\text{Cr}^{4+}$  species persists, and two reduced Cr cations are reduced to  $\text{Cr}^{2+}$ . The  $\text{Ti}^{3+}$  species found in the stoichiometric composite persists; the computed Bader charge is 1.73 electrons, and the spin magnetization is  $0.98 \mu_B$ . Thus, two Cr cations in the nanocluster are reduced from  $\text{Cr}^{3+}$  to  $\text{Cr}^{2+}$  and no further Ti reduction takes place.

If we examine the PEDOS plots for the stoichiometric systems, we see that there are empty Cr 3d states lying at the  $\text{TiO}_2$  conduction band edge so that electrons can be accommodated in these states. The chromia nanoclusters can undergo more distortion than the  $\text{TiO}_2$  surfaces upon reduction of Cr in the nanocluster and thus it is generally more favorable for an electron to localize onto Cr sites than onto surface Ti sites.

**2.4. Effect of Surface Water on Adsorption of Chromia Nanoclusters on  $\text{TiO}_2$ .** In this section, we extend the description of  $\text{Cr}_2\text{O}_3$ -modified  $\text{TiO}_2$  surfaces by including the effect of a surface in which water is present before the nanocluster is adsorbed. This analysis can provide insights into the effect of more realistic environmental conditions, where water is always present. Water adsorption on oxide surfaces has been well-studied, for example, refs 43–46, 63, and 64. In a previous study, we found that the presence of water, which we model as adsorbed hydroxyls on rutile (110),<sup>30</sup> can change the properties of  $\text{TiO}_2$  nanocluster-modified rutile (110). For example, we found no red shift upon  $\text{TiO}_2$  nanocluster modification of a hydroxylated rutile (110) surface,<sup>30</sup> in

contrast to the modification of a perfect rutile (110) surface with the same nanocluster.<sup>55</sup> We attributed this to the passivation of singly coordinated titanyl oxygen species with hydrogen that migrated from the surface hydroxyls to the nanocluster. This passivation lowers the energy of the  $\text{TiO}_2$  nanocluster states that were responsible for the narrowing of the energy gap.

For the rutile (110) and anatase (101) surfaces, we use a water coverage of 1/2 ML, which consists of four dissociated water molecules adsorbed as surface-bound hydroxyls. The aim here is not to analyze the most stable coverage and structure of water on the respective  $\text{TiO}_2$  surfaces but to use a typical water adsorption structure to compare with nanocluster modification of the corresponding dry  $\text{TiO}_2$  surface. The computed adsorption energies for  $\text{Cr}_4\text{O}_6$  adsorbed on each wet surface are  $-1.08$  eV on rutile (110) and  $-2.21$  eV on anatase (101). Although these are reduced compared with  $\text{Cr}_4\text{O}_6$  nanocluster adsorption on the nonhydroxylated rutile and anatase surfaces, they nonetheless indicate that the chromia nanoclusters can also adsorb at hydroxylated  $\text{TiO}_2$  surfaces.

Figure 6 shows the relaxed geometry of rutile (110) and anatase (101) surfaces with 1/2 ML water coverage after the adsorption of the  $\text{Cr}_4\text{O}_6$  nanocluster. The interatomic distances are shown in Figure S5, Supporting Information, and the structures are discussed in detail in the Supporting Information. After structural relaxation, we observe proton migration from surface OH groups (both terminal and bridging hydroxyls) to the adsorbed nanocluster. New O–H bonds are formed with nanocluster oxygen, with typical O–H distances of  $0.98$ – $1.0$  Å. On hydroxylated rutile (110), three protons from surface hydroxyls migrate to produce hydroxyl bonds, whereas on hydroxylated anatase (101), two hydrogen atoms migrate from

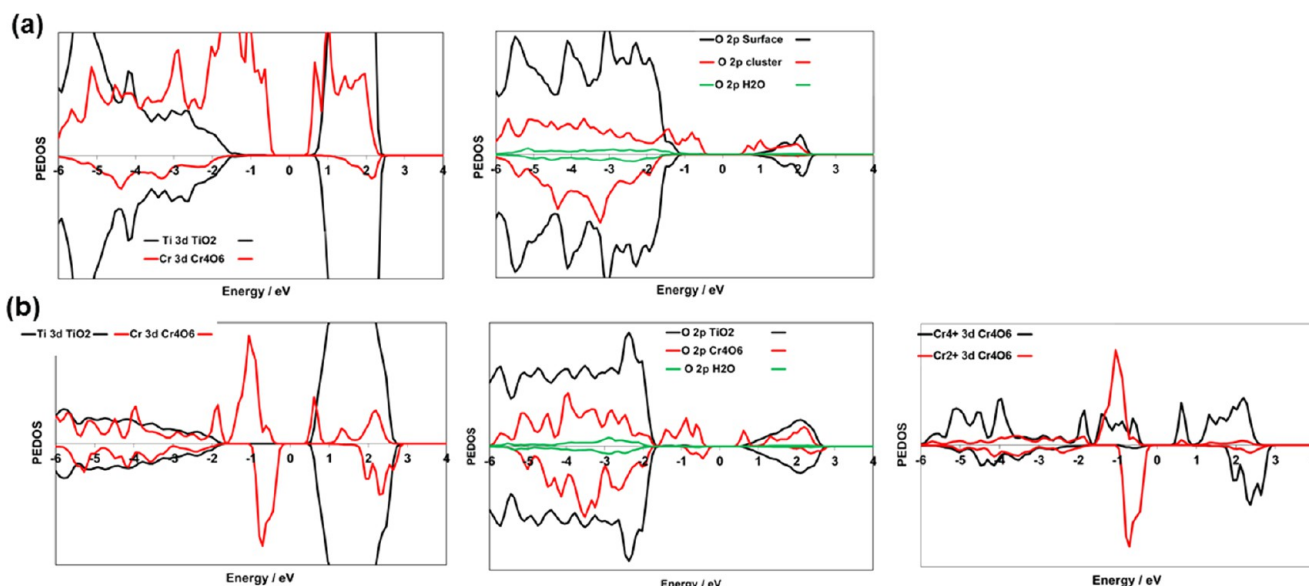


**Figure 7.** Projected electronic density of states (PEDOSs) projected onto the Ti 3d and Cr 3d states in the  $\text{Cr}_2\text{O}_3$ – $\text{TiO}_2$  composites with a water coverage of 1/2 ML on each  $\text{TiO}_2$  surface (left column), the O 2p states of the adsorbed chromia nanoclusters and  $\text{TiO}_2$  surfaces (middle column), and Ti 3d and Cr 3d states for Ti and Cr species with oxidation states other than  $\text{Ti}^{4+}$  and  $\text{Cr}^{3+}$  (right column). (a)  $\text{Cr}_4\text{O}_6$ -modified rutile (110) and (b)  $\text{Cr}_4\text{O}_6$ -modified anatase (101). The zero of energy is the Fermi level.

**Table 3. Computed Oxygen Vacancy Formation Energies in the  $\text{Cr}_4\text{O}_6$  Nanocluster-Modified Wet Rutile (110) and Anatase (101)  $\text{TiO}_2$  Surfaces, with 1/2 ML Water Coverage<sup>a</sup>**

O vacancy site $\text{Cr}_4\text{O}_6$ -hydroxylated rutile (110)	O vacancy formation energy/eV	O vacancy site $\text{Cr}_4\text{O}_6$ -hydroxylated anatase (101)	O vacancy formation energy/eV
I	4.86	I	1.72
II	3.61	II	2.16
III	4.59	III	3.05
IV	<b>0.69</b>	IV	<b>1.35</b>
V	2.79	V	3.68
VI	3.32	VI	1.58

<sup>a</sup>The values in bold font show the most stable oxygen vacancy sites.

the surface hydroxyls to make new OH bonds with the nanocluster.

On rutile (110), there are two Ti–O bonds between Ti in the surface and oxygen in the nanocluster, with Ti–O distances of 1.83 and 1.98 Å. The former atom migrated by 0.9 Å from its surface lattice site to make a bridging bond with the nanocluster. The Cr–O distances to the bridging oxygen in the surface are 1.95 and 1.82/1.91 Å; the longer Cr–O bond is to the bridging hydroxyl oxygen. Within the nanocluster, Cr–O distances range from 1.78 to 2.07 Å, with the lower coordinated Cr atoms showing the shorter Cr–O distances. Finally, the Cr–O distances to the hydroxyl oxygen are 1.80, 1.81, and 1.98 Å.

In the  $\text{Cr}_4\text{O}_6$ -anatase system, two protons have migrated from the surface hydroxyl groups to bind with the oxygen in the  $\text{Cr}_4\text{O}_6$  nanocluster. There are four Cr–O bonds between the nanocluster and the surface. A 4-fold-coordinated square planar Cr atom binds to two surface oxygens in anatase (101), with a Cr–O distance of 2.06 Å, and to a surface hydroxyl, with a Cr–O distance of 2.06 Å. Another 4-fold-coordinated, square planar Cr atom binds to an original hydroxyl oxygen, with a Cr–O distance of 2.0 Å. The final, tetrahedrally coordinated, Cr atom has a Cr–O distance of 1.97 Å to a hydroxyl oxygen. Within the nanocluster, Cr–O distances are in the range of 1.62 Å (chromyl oxygen) and 1.71 Å (3-fold-coordinated Cr) to 2.08 Å.

On  $\text{Cr}_4\text{O}_6$ -rutile (110), at 1/2 ML water coverage, there is no formation of reduced  $\text{Ti}^{3+}$  species, all Ti atoms have computed Bader charges of 1.3 electrons and zero spin magnetizables. The computed Bader charges on Cr are all 10.3 electrons, with corresponding spin magnetizables of  $3 \mu_B$ , which is consistent with the presence of  $\text{Cr}^{3+}$  species. In  $\text{Cr}_4\text{O}_6$ -anatase, the computed Cr Bader charges are 10.53, 10.3, 10.53, and 10.1 electrons, with spin magnetizables of 3.6, 2.4, 3.6, and  $2 \mu_B$ . The Ti Bader charges are 1.27–1.32 electrons with zero spin magnetization, indicating that only  $\text{Ti}^{4+}$  species are present. The Cr Bader charges and spin magnetizables indicate that oxidation states other than  $\text{Cr}^{3+}$  are present. From these data, we propose a charge disproportionation as follows:  $4\text{Cr}^{3+} \rightarrow 2\text{Cr}^{2+} + 2\text{Cr}^{4+}$ , so that no Ti sites are reduced. We note that the  $\text{Cr}^{4+}$  sites are 3-fold-coordinated and the reduced  $\text{Cr}^{2+}$  sites are 4-fold-coordinated.

The PEDOS plots in Figure 7 show similar general features to those of the  $\text{Cr}_4\text{O}_6$ -modified perfect surfaces. There are chromia-derived electronic states lying above the valence band edge of the  $\text{TiO}_2$  surfaces. On hydroxylated anatase, the  $\text{Cr}^{2+}$  states dominate the top of the valence band region, whereas the empty  $\text{Cr}^{4+}$  states dominate the bottom of the conduction band. In contrast to the dry anatase (101) surface, the PEDOS further confirms that there are no reduced  $\text{Ti}^{3+}$  species present with adsorbed water on the  $\text{TiO}_2$  surface. Thus, the presence of



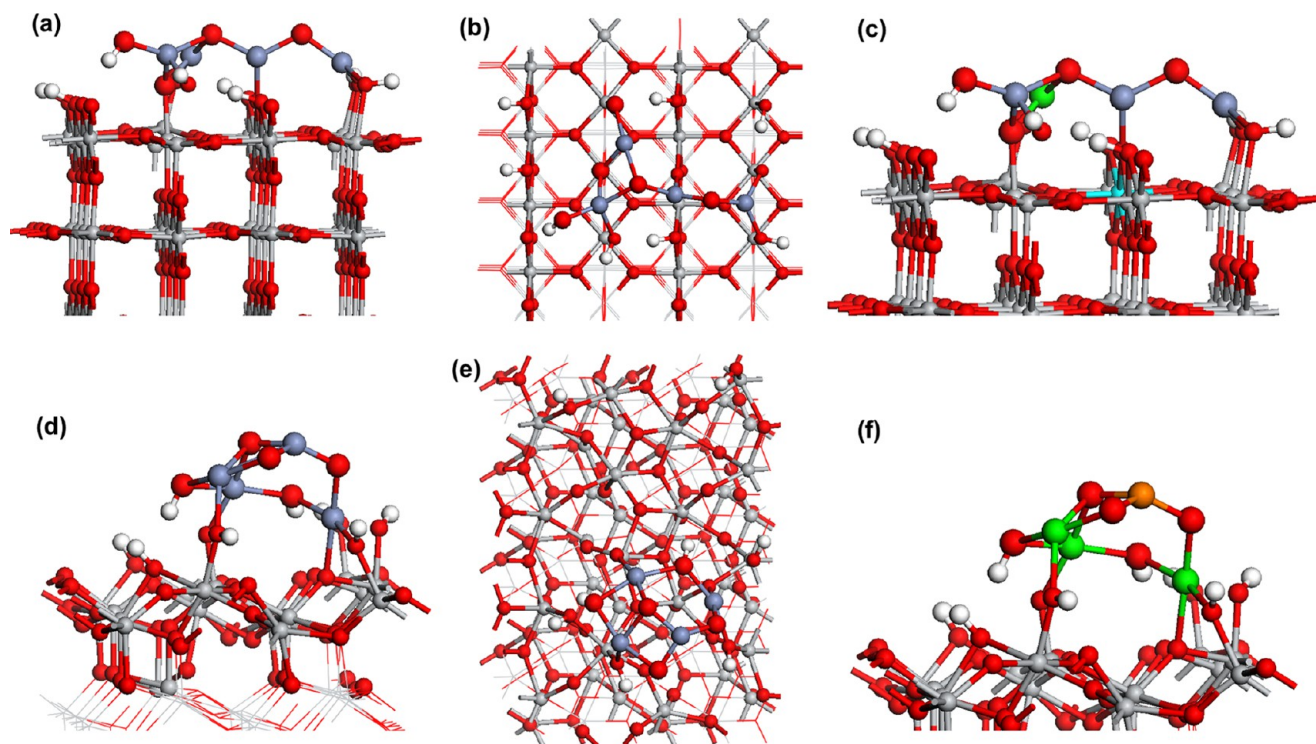


**Figure 8.** Atomic structure of  $\text{Cr}_4\text{O}_6$  nanoclusters adsorbed on the  $\text{TiO}_2$  rutile (110) and  $\text{TiO}_2$  anatase (101) surfaces with 1/2 ML water coverage, after formation of the most stable oxygen vacancy in the nanocluster. The left panels show a side view, the middle panels show a plan view, and the right panels show the location of  $\text{Ti}^{3+}$ ,  $\text{Cr}^{4+}$ , and  $\text{Cr}^{2+}$  species, which are cyan, orange, and green, respectively. Structures representing (a–c)  $\text{Cr}_4\text{O}_6$  adsorbed on rutile (110) and (d–f)  $\text{Cr}_4\text{O}_6$  adsorbed on anatase (101).

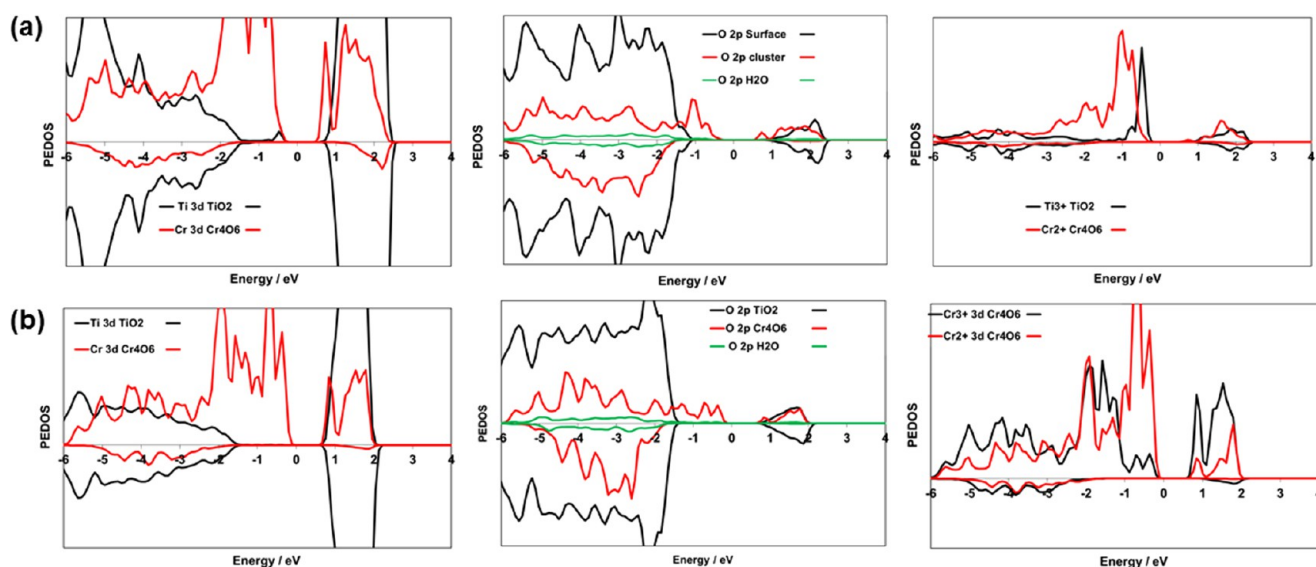


**Figure 9.** Projected electronic density of states (PEDOSs) projected onto the Ti 3d and Cr 3d states in the  $\text{Cr}_2\text{O}_3$ – $\text{TiO}_2$  composites with a water coverage of 1/2 ML on each  $\text{TiO}_2$  surface and an oxygen vacancy in the chromia nanocluster (left column), the O 2p states of the adsorbed chromia nanoclusters and  $\text{TiO}_2$  surfaces (middle column), and Ti 3d and Cr 3d states for Ti and Cr species with oxidation states other than  $\text{Ti}^{4+}$  and  $\text{Cr}^{3+}$  (right column). (a)  $\text{Cr}_4\text{O}_6$ -modified rutile (110) and (b)  $\text{Cr}_4\text{O}_6$ -modified anatase (101). The zero of energy is the Fermi level.

water on the modified  $\text{TiO}_2$  surface has no impact on the predicted red shift of the absorption edge.

**2.5. Formation of Oxygen Vacancies in  $\text{Cr}_4\text{O}_6$ -Modified Rutile (110) and Anatase (101).** Similar to the modified perfect rutile and anatase surfaces, we have analyzed oxygen vacancy formation by removing each oxygen in the nanocluster and computing the formation energy, as given in Table 3. The numbering of the oxygen vacancy sites is given in

Figure S6, Supporting Information. The most stable oxygen vacancies have formation energies of +0.69 eV in  $\text{Cr}_4\text{O}_6$ -rutile (110) and +1.35 eV in  $\text{Cr}_4\text{O}_6$ -anatase (101), which are suggestive of significant reducibility in chromia-modified rutile and anatase, so that this aspect of chromia-modified  $\text{TiO}_2$  is not impacted by the presence of water on the  $\text{TiO}_2$  surface.

Figure 8 shows the atomic structure of  $\text{Cr}_4\text{O}_6$ -modified hydroxylated rutile (110) and anatase (101) after formation of



the most stable oxygen vacancy. The interatomic distances are shown in Figure S7, and the structures are discussed in the Supporting Information. In  $\text{Cr}_4\text{O}_6$ -rutile (110), the formation of the vacancy does not induce significant structural distortions compared to those in the unhydroxylated surface. This is seen in the larger oxygen vacancy formation energy when the surface is hydroxylated. Two Ti–nanocluster bonds persist, with distances of 2.02 and 1.85 Å, with the latter involving the surface Ti atom that migrates out of the surface. There is a 3-fold-coordinated Cr that binds to the bridging surface oxygen, with a Cr–O distance of 1.86 Å. A second Cr atom binds to a hydroxyl oxygen and an oxygen, with Cr–O distances of 1.80 Å (to oxygen) and 1.89 Å (to hydroxyl oxygen). The remaining Cr has Cr–O distances in the cluster of 1.81 and 1.96 Å to the hydroxyl oxygen and 1.93, 1.95, 2.04, and 2.06 Å to oxygen.

On modified hydroxylated anatase (101), the most stable vacancy site in the nanocluster is not the chromyl oxygen site, which was passivated by migration of hydrogen from the surface hydroxyl to the nanocluster. A 3-fold-coordinated Cr cation binds to two hydroxyl groups in the nanocluster with Cr–O distances of 1.83 Å to the terminal hydroxyl and 1.92 Å to a bridging hydroxyl (the second Cr–OH distance is 2.04 Å). A 4-coordinate Cr cation has Cr–O distances to surface hydroxyls of 1.97 and 1.96 Å, whereas the other 4-fold-coordinated Cr cation has Cr–O distances of 2.03 and 2.07 Å to the surface, binding to the surface oxygen and hydroxyls, respectively. Finally, there are no surface Ti-to-nanocluster bonds.

The computed Bader charges show that in  $\text{Cr}_4\text{O}_6$ -rutile the formation of the oxygen vacancy leads to the reduction of a surface Ti cation and a nanocluster Cr cation. These have computed Bader charges of 1.66 and 10.6 electrons, with computed spin magnetizables of 0.94 and 3.7  $\mu_B$ , consistent with  $\text{Ti}^{3+}$  and  $\text{Cr}^{2+}$  oxidation states. Upon formation of the oxygen vacancy in  $\text{Cr}_4\text{O}_6$ -anatase (101), there are no reduced  $\text{Ti}^{3+}$  states formed. Instead, two  $\text{Cr}^{4+}$  cations are each reduced to  $\text{Cr}^{3+}$  and the remaining Cr cations maintain their  $\text{Cr}^{2+}$  oxidation states. The computed Bader charge on the  $\text{Cr}^{2+}$  cations are 10.8 and 10.7 electrons, with a spin magnetization of 3.6  $\mu_B$ . The  $\text{Cr}^{3+}$  cations have Bader charges of 10.1 and 10.2 electrons with spin magnetizables of 3  $\mu_B$ .

Figure 9 shows the PEDOS projected onto the Ti 3d, Cr 3d, and O 2p electronic states in  $\text{Cr}_4\text{O}_6$ -rutile and  $\text{Cr}_4\text{O}_6$ -anatase from the most stable oxygen vacancy structures. In  $\text{Cr}_4\text{O}_6$ -rutile (110), the  $\text{Cr}_4\text{O}_6$  electronic states that moved the valence band to a higher energy persist and there is a new  $\text{Ti}^{3+}$ -derived electronic state that lies 1 eV above the valence band edge of the surface. The PEDOS also shows the presence of  $\text{Cr}^{2+}$  states resulting from Cr reduction after vacancy formation. In  $\text{Cr}_4\text{O}_6$ -anatase (101), formation of the oxygen vacancy does not produce any  $\text{Ti}^{3+}$  electronic states in the energy gap, consistent with the computed Bader charges. The different Cr oxidation states are apparent in the PEDOS plot, with  $\text{Cr}^{2+}$  states dominating at the valence band edge and empty  $\text{Cr}^{4+}$  states dominating at the conduction band edge.

### 3. CONCLUSIONS

We have used DFT +  $U$  to study  $\text{TiO}_2$  rutile (110) and anatase (101) surfaces modified with chromia nanoclusters, taking into partial account the effect of the state of the surface by modeling perfect and hydroxylated rutile and anatase surfaces (with a water coverage of 1/2 monolayer). We have investigated the stability, structure, electronic properties, oxidation states, and

reducibility of these composite systems. All nanocluster-modified surface composites are stable, as determined by the computed adsorption energies. The surface hydroxylation reduces the magnitude of the adsorption energy, arising from the migration of hydrogen from surface hydroxyl to the nanocluster and longer surface–nanocluster distances. The composites show enhanced reducibility compared to that for the unmodified  $\text{TiO}_2$  surfaces, irrespective of the state of the  $\text{TiO}_2$  surfaces, although the hydroxylated surfaces show slightly larger formation energies and vacancy formation is more favorable on chromia–rutile than on chromia–anatase.

The electronic structure shows that chromia modifications will red-shift light absorption due to the presence of chromia-derived electronic states that lie above the valence band edge of  $\text{TiO}_2$ . For a  $\text{Cr}_4\text{O}_6$  nanocluster on dry anatase (101),  $\text{Ti}^{3+}$  and  $\text{Cr}^{4+}$  species are present, but for the same nanocluster on dry rutile (110), all Cr is in the +3 oxidation state and all Ti is in the +4 oxidation state. Similarly, on hydroxylated  $\text{TiO}_2$  surfaces, oxidation states other than  $\text{Ti}^{3+}$  and  $\text{Cr}^{4+}$  can be present.

On examining the photoexcited state, we find that upon electron and hole formation the electron and hole localization can depend on the  $\text{TiO}_2$  surface. For modified rutile (110), the charges localize on the chromia nanocluster, whereas on anatase (101), the charges separate onto the nanocluster and the  $\text{TiO}_2$  surface. In both cases, there is a clear red shift in the singlet–triplet energies, indicative of a red shift in the absorption edge.

These results show that modification of rutile or anatase with chromia nanoclusters can be used to red-shift light absorption and induce reducibility in these composite structures. The effect of water on the key properties of these composites is not notably strong. These results also allow us to understand the experimental work of Irie et al., including their observed red shift and electron transfer to chromia.

### 4. CALCULATION METHODS

The calculations presented in this work are performed using a density functional theory approach, within three-dimensional periodic boundary conditions with a plane wave basis set to describe the valence electron wave functions, as implemented in the VASP5.2 code.<sup>65,66</sup> The PW91 generalized gradient approximation (GGA) to the exchange–correlation functional<sup>67</sup> is used. We use a plane wave cutoff energy of 396 eV. The core–valence electron interaction is described by the projector augmented wave approach,<sup>68</sup> in which we use 4 valence electrons for Ti, 6 for O, 12 for Cr, and 1 electron for H atoms. Methfessel–Paxton smearing with  $\sigma = 0.1$  eV is used in structure relaxations, and energies are obtained for  $\sigma \rightarrow 0$ . A  $(2 \times 2 \times 1)$  Monkhorst–Pack  $k$ -point sampling grid has been used for a  $(2 \times 4)$  expansion of the  $\text{TiO}_2$  rutile (110) surface and a  $(4 \times 2)$  expansion of the anatase (101) surface. These have 18 and 12 atomic layers and a vacuum gap of 20 Å. The convergence criteria for the energy and forces are  $10^{-5}$  eV and  $2 \times 10^{-2}$  eV Å<sup>−2</sup>, respectively.

To correctly describe the partially occupied Ti 3d, Cr 3d, and O 2p electronic states, a Hubbard correction for the exchange–correlation potential has been employed. The Ti 3d states are described with  $U$  (Ti 3d) = 4.5 eV. In describing localized oxygen 2p states, we follow previous work and set  $U$  (O 2p) = 5.5 eV.<sup>30,31</sup> The use of the Hubbard +  $U$  correction on the Ti 3d states becomes crucial when  $\text{Ti}^{3+}$  species form, and it gives a consistent description of the electronic states and any polaronic defects that can form in these systems. In addition, in previous

studies, we found that this correction is necessary to describe O 2p states that result after valence band hole formation.<sup>30,31,69</sup> Finally, the partially filled 3d states in Cr also require a DFT + *U* correction to be consistently described, and here, we use *U* (Cr 3d) = 3.5 eV,<sup>60</sup> consistent with values used in other studies.

To analyze possible excited states, we perform a calculation in which we impose a triplet electronic state on the chromia–TiO<sub>2</sub> system. This allows us to model an “excited” electron in the conduction band (and a hole in the valence band), thus mimicking photoexcited states. Three fundamental energies can be computed within this approach:

$E^{\text{vertical}}$ , which is computed as the energy difference between the relaxed singlet ground state and the unrelaxed triplet electronic state; this corresponds to the simple valence–conduction band energy difference from the singlet ground state;

$E^{\text{S–T}}$ , which is computed from the energy difference between the relaxed singlet ground state and the relaxed triplet electronic state (i.e., the geometry is allowed to relax in response to occupying a conduction band state with a corresponding valence band hole); this can be thought of as an excitation energy and indicates the effect of the surface modification on the absorption edge;

$E^{\text{relax}}$ , which is the energy difference between the unrelaxed triplet electronic state and the relaxed triplet electronic state; this is the energy gained when the structure relaxes upon trapping of the excited electron and the hole at preferred lattice sites and gives an indication of the stability of trapped electrons and holes.

A more detailed description of this methodology in the context of surface-modified TiO<sub>2</sub> can be found elsewhere.<sup>30,31,51</sup> Of course, this is a very simple model of the photoexcited state and we cannot say anything about the lifetime of photoexcited electrons and holes and which processes, such as de-excitation or electron transfer, will dominate in these systems. Nonetheless, we can obtain useful information regarding the preferred location of photogenerated electrons and holes and their stability.

In the present composite structures, we have found that the most stable spin state is always that with the highest spin, which can be up to 0.5 eV more stable than low-spin solutions. Thus, there is an overall spin of 6 on Cr<sub>2</sub>O<sub>3</sub> and a spin of 12 on Cr<sub>4</sub>O<sub>6</sub> (3 spins per Cr cation). Thus, in the triplet electronic state, we set the number of excess up-spin electrons to 14.

## ■ ASSOCIATED CONTENT

### ■ Supporting Information

The Supporting Information is available free of charge on the ACS Publications website at DOI: 10.1021/acsomega.7b01118.

Adsorption structure for less stable isomers of chromia-modified TiO<sub>2</sub>; interatomic distances for Cr<sub>2</sub>O<sub>3</sub>-nanocluster-modified rutile (110), Cr<sub>4</sub>O<sub>6</sub>-rutile (110), and Cr<sub>4</sub>O<sub>6</sub>-anatase (101); numbering of oxygen vacancy sites for Cr<sub>4</sub>O<sub>6</sub>-rutile (110) and Cr<sub>4</sub>O<sub>6</sub>-anatase (101); interatomic distances for the most stable oxygen vacancy site in Cr<sub>4</sub>O<sub>6</sub>-nanocluster-modified rutile (110) and Cr<sub>4</sub>O<sub>6</sub>-anatase (101); interatomic distances for Cr<sub>4</sub>O<sub>6</sub>-nanocluster-modified hydroxylated rutile (110) and Cr<sub>4</sub>O<sub>6</sub>-nanocluster-modified hydroxylated anatase (101); numbering of oxygen vacancy sites for Cr<sub>4</sub>O<sub>6</sub>-hydroxylated rutile (110) and Cr<sub>4</sub>O<sub>6</sub>-hydroxylated anatase (101); interatomic distances for the most stable

oxygen vacancy site in Cr<sub>4</sub>O<sub>6</sub>-nanocluster-modified hydroxylated rutile (110) and Cr<sub>4</sub>O<sub>6</sub>-nanocluster-modified hydroxylated anatase (101); detailed descriptions of the geometry of each composite system (PDF)

## ■ AUTHOR INFORMATION

### Corresponding Author

\*E-mail: michael.nolan@tyndall.ie.

### ORCID

Michael Nolan: 0000-0002-5224-8580

### Present Address

<sup>†</sup>International Research Centre for Renewable Energy, State Key Laboratory of Multiphase Flow in Power Engineering, Xi'an Jiaotong University, Xi'an 710049, Shaanxi, China (M.F.).

### Notes

The authors declare no competing financial interest.

## ■ ACKNOWLEDGMENTS

We acknowledge support from the Science Foundation Ireland (SFI) through the US-Ireland R&D Partnership Program, grant number SFI 14/US/E2915 and the European Commission through the COST Action CM1104 “Reducible Metal Oxides, Structure and Function”. We acknowledge access to computing resources at Tyndall provided by SFI and by the SFI and Higher Education Authority funded Irish Centre for High End Computing.

## ■ REFERENCES

- (1) Pelaez, M.; Nolan, N. T.; Byrne, J. A.; Pillai, S. C.; Seery, M. K.; Falaras, P.; Kontos, A. G.; Dunlop, P. S. M.; Hamilton, J. W. J.; O'Shea, K.; Entezari, M. H.; Dionysiou, D. D. A review on the visible light active titanium dioxide photocatalysts for environmental applications. *Appl. Catal., B* **2012**, *125*, 331–349.
- (2) Pillai, S. C.; Stangar, U. L.; Byrne, J. A.; Pérez-Larios, A.; Dionysiou, D. D. Photocatalysis for disinfection and removal of contaminants of emerging concern. *Chem. Eng. J.* **2015**, *261*, 1–2.
- (3) Etacheri, V.; Di Valentin, C.; Schneider, J.; Bahnemann, D.; Pillai, S. C. Visible-light activation of TiO<sub>2</sub> photocatalysts: Advances in theory and experiments. *J. Photochem. Photobiol., C* **2015**, *25*, 1–29.
- (4) Diebold, U. The surface science of titanium dioxide. *Surf. Sci. Rep.* **2003**, *48*, 53–229.
- (5) Fuerte, A.; Hernández-Alonso, M. D.; Maira, A. J.; Martínez-Arias, A.; Fernández-García, M.; Conesa, J. C.; Soria, J. Visible light-activated nanosized doped-TiO<sub>2</sub> photocatalysts. *Chem. Commun.* **2001**, 2718–2729.
- (6) Li, W. Influence of electronic structures of doped TiO<sub>2</sub> on their photocatalysis. *Phys. Status Solidi RRL* **2015**, *9*, 10–27.
- (7) Anpo, M. Use of visible light. Second-generation titanium oxide photocatalysts prepared by the application of an advanced metal ion-implantation method. *Pure Appl. Chem.* **2000**, *72*, 1787–1792.
- (8) Ozawa, K.; Emori, M.; Yamamoto, S.; Yukawa, R.; Hobara, R.; Fujikawa, K.; Sakama, H.; Matsuda, I.; Yamamoto, S. Electron–hole recombination time at TiO<sub>2</sub> single-crystal surfaces: Influence of surface band bending. *J. Phys. Chem. Lett.* **2014**, *5*, 1953–1957.
- (9) Serpone, N. Is the band gap of pristine TiO<sub>2</sub> narrowed by anion- and cation-doping of titanium dioxide in second-generation photocatalysts? *J. Phys. Chem. B* **2006**, *110*, 24287–24293.
- (10) Phattalung, S. N.; Limpijumnong, S.; Yu, J. Passivated co-doping approach to bandgap narrowing of titanium dioxide with enhanced photocatalytic activity. *Appl. Catal., B* **2017**, *200*, 1–9.
- (11) Wang, P.; Liu, Z.; Lin, F.; Zhou, G.; Wu, J.; Duan, W.; Gu, B.-L.; Zhang, S. B. Optimizing photoelectrochemical properties of TiO<sub>2</sub> by chemical codoping. *Phys. Rev. B* **2010**, *82*, No. 193103.
- (12) Zhang, D.; Yang, M. Band structure engineering of TiO<sub>2</sub> nanowires by n–p codoping for enhanced visible-light photo-

electrochemical water-splitting. *Phys. Chem. Chem. Phys.* **2013**, *15*, 18523–18529.

(13) Wang, J.; Sun, H.; Huang, J.; Li, Q.; Yang, J. Band structure tuning of TiO<sub>2</sub> for enhanced photoelectrochemical water splitting. *J. Phys. Chem. C* **2014**, *118*, 7451–7457.

(14) Asahi, R.; Morikawa, T.; Ohwaki, K.; Aoki, K.; Taga, Y. Visible-Light photocatalysis in nitrogen-doped titanium oxides. *Science* **2001**, *293*, 269–271.

(15) Xing, M.; Wu, Y.; Zhang, J.; Chen, F. Effect of synergy on the visible light activity of B, N and Fe co-doped TiO<sub>2</sub> for the degradation of MO. *Nanoscale* **2010**, *2*, 1233–1239.

(16) Di Valentin, C.; Pacchioni, G. Trends in non-metal doping of anatase TiO<sub>2</sub>: B, C, N and F. *Catal. Today* **2013**, *206*, 12–18.

(17) Gai, Y.; Li, J.; Li, S.-S.; Xai, J.-B.; Wei, S.-H. Design of narrow-gap TiO<sub>2</sub>: A passivated codoping approach for enhanced photoelectrochemical activity. *Phys. Rev. Lett.* **2009**, *102*, No. 036402.

(18) Peng, Y.-H.; Huang, G.-F.; Huang, W.-Q. Visible-light absorption and photocatalytic activity of Cr-doped TiO<sub>2</sub> nanocrystal films. *Adv. Powder Technol.* **2012**, *23*, 8–12.

(19) Li, X.; Guoa, Z.; He, T. The doping mechanism of Cr into TiO<sub>2</sub> and its influence on the photocatalytic performance. *Phys. Chem. Chem. Phys.* **2013**, *15*, 20037–20045.

(20) Ghicov, A.; Schmidt, B.; Kunze, J.; Schmuki, P. Photoresponse in the visible range from Cr doped TiO<sub>2</sub> nanotubes. *Chem. Phys. Lett.* **2007**, *433*, 323–326.

(21) Herrmann, J.-M.; Disdier, J.; Pichat, P. Effect of chromium doping on the electrical and catalytic properties of powder titania under UV and visible illumination. *Chem. Phys. Lett.* **1984**, *108*, 618–622.

(22) Yu, X.; Kim, B.; Kim, Y. K. Highly enhanced photoactivity of anatase TiO<sub>2</sub> nanocrystals by controlled hydrogenation-induced surface defects. *ACS Catal.* **2013**, *3*, 2479–2486.

(23) Wang, Z.; Liu, Y.; Huang, B.; Dai, Y.; Lou, Z.; Wang, G.; Zhang, X.; Qin, X. Progress on extending the light absorption spectra of photocatalysts. *Phys. Chem. Chem. Phys.* **2014**, *16*, 2758–2784.

(24) Chen, X.; Liu, L.; Liu, Z.; Marcus, M. A.; Wang, W.-C.; Oyler, N. A.; Grass, M. E.; Mao, B.; Glans, P.-A.; Yu, P. Y.; Guo, J.; Mao, S. S. Properties of disorder-engineered black titanium dioxide nanoparticles through hydrogenation. *Sci. Rep.* **2013**, *3*, No. 1510.

(25) Harris, C.; Kamat, P. V. Photocatalysis with CdSe nanoparticles in confined media: mapping charge transfer events in the subpicosecond to second timescales. *ACS Nano* **2009**, *3*, 682–690.

(26) Yun, H. J.; Paik, T.; Diroll, B.; Edley, M. E.; Baxter, J. B.; Murray, C. B. Nanocrystal size-dependent efficiency of quantum dot sensitized solar cells in the strongly coupled CdSe nanocrystals/TiO<sub>2</sub> system. *ACS Appl. Mater. Interfaces* **2016**, *8*, 14692–14700.

(27) Chen, J.-J.; Wu, J. C. S.; Wu, P. C.; Tsai, D. P. Plasmonic photocatalyst for H<sub>2</sub> evolution in photocatalytic water splitting. *J. Phys. Chem. C* **2011**, *115*, 210–216.

(28) Zhao, H.; Huang, F.; Hou, J.; Liu, Z.; Wu, Q.; Cao, H.; Jing, Q.; Peng, S.; Cao, G. Efficiency enhancement of quantum dot sensitized TiO<sub>2</sub>/ZnO nanorod array solar cells by plasmonic Ag nanoparticles. *ACS Appl. Mater. Interfaces* **2016**, *8*, 26675–26682.

(29) Tada, H.; Qin, J.; Iwaszuk, A.; Nolan, M. Molecular scale transition metal oxide nanocluster surface-modified titanium dioxide as solar-activated environmental catalysts. *J. Phys. Chem. C* **2014**, *118*, 12077–12086.

(30) Fronzi, M.; Iwaszuk, A.; Lucid, A. K.; Nolan, M. Metal oxide nanocluster-modified TiO<sub>2</sub> as solar activated photocatalyst materials. *J. Phys.: Condens. Matter* **2016**, *28*, No. 074006.

(31) Nolan, M.; Iwaszuk, A.; Lucid, A. K.; Carey, J. J.; Fronzi, M. Design of novel visible light active photocatalyst materials: surface modified TiO<sub>2</sub>. *Adv. Mater.* **2016**, *28*, 5425–5446.

(32) Sahoo, C.; Gupta, A. K. Characterisation and photocatalytic performance evaluation of various metal doped microstructured TiO<sub>2</sub> under UV and visible light. *J. Environ. Sci. Health, Part A: Toxic/Hazard. Subst. Environ. Eng.* **2015**, *50*, 659–668.

(33) Liu, J.; Zhang, Q.; Yang, J.; Ma, H.; Tade, M. O.; Wang, S.; Liu, J. Facile synthesis of carbon-doped mesoporous anatase TiO<sub>2</sub> for the

enhanced visible-light driven photocatalysis. *Chem. Commun.* **2014**, *50*, 13971–13974.

(34) Tada, H.; Jin, Q.; Nishijima, H.; Yamamoto, H.; Fujishima, M.; Okuoka, S.-i.; Hattori, T.; Sumida, Y.; Kobayashi, H. Titanium(IV) oxide surface-modified with iron oxide as a visible light photocatalyst. *Angew. Chem., Int. Ed. Engl.* **2011**, *50*, 3501–3505.

(35) Jin, Q.; Fujishima, M.; Tada, H. Visible-light-active iron oxide-modified anatase titanium(IV) dioxide. *J. Phys. Chem. C* **2011**, *115*, 6478–6483.

(36) Irie, H.; Shibamura, T.; Kamiya, K.; Miura, S.; Yokoyama, T.; Hashimoto, K. Characterization of Cr(III)-grafted TiO<sub>2</sub> for photocatalytic reaction under visible light. *Appl. Catal., B* **2010**, *96*, 142–147.

(37) Nolan, M. Surface modification of TiO<sub>2</sub> with metal oxide nanoclusters: a route to composite photocatalytic materials. *Chem. Commun.* **2011**, *47*, 8617–8619.

(38) Iwaszuk, A.; Nolan, M. SnO-nanocluster modified anatase TiO<sub>2</sub> photocatalyst: exploiting the Sn(II) lone pair for a new photocatalyst material with visible light absorption and charge carrier separation. *J. Mater. Chem. A* **2013**, *1*, 6670–6677.

(39) Iwaszuk, A.; Nolan, M. Lead oxide-modified TiO<sub>2</sub> photocatalyst: tuning light absorption and charge carrier separation by lead oxidation state. *Catal. Sci. Technol.* **2013**, *3*, 2000–2008.

(40) Patel, M.; Sanches, F. F.; Mallia, G.; Harrison, N. M. A quantum mechanical study of water adsorption on the (110) surfaces of rutile SnO<sub>2</sub> and TiO<sub>2</sub>: investigating the effects of intermolecular interactions using hybrid-exchange density functional theory. *Phys. Chem. Chem. Phys.* **2014**, *16*, 21002–21015.

(41) Patel, M.; Mallia, G.; Liborio, L.; Harrison, N. M. Water adsorption on rutile TiO<sub>2</sub> (110) for applications in solar hydrogen production: A systematic hybrid-exchange density functional study. *Phys. Rev. B* **2012**, *86*, No. 045302.

(42) Sahoo, S. K.; Nigam, S.; Sarkar, P.; Majumder, C. DFT study of H<sub>2</sub>O adsorption on TiO<sub>2</sub> (110) and SnO<sub>2</sub> (110) surfaces. *AIP Conf. Proc.* **2013**, *1512*, 292–293.

(43) Zhao, Z.-Y. Single water molecule adsorption and decomposition on the low-index stoichiometric rutile TiO<sub>2</sub> surfaces. *J. Phys. Chem. C* **2014**, *118*, 4287–4295.

(44) Sun, C.; Liu, L.-M.; Selloni, A.; Lu, G. Q.; Smith, S. C. Titania–water interactions: a review of theoretical studies. *J. Mater. Chem.* **2010**, *20*, 10319–10334.

(45) Kristoffersen, H. H.; Hansen, J. Ø.; Martinez, U.; Wei, Y. Y.; Matthiesen, J.; Bechstein, R.; Lægsgaard, E.; Besenbacher, F.; Hammer, B.; Wendt, S.; Streber, R. Role of steps in the dissociative adsorption of water on rutile TiO<sub>2</sub> (110). *Phys. Rev. Lett.* **2013**, *110*, No. 146101.

(46) Tilocca, A.; Selloni, A. DFT–GGA and DFT+U simulations of thin water layers on reduced TiO<sub>2</sub> anatase. *J. Phys. Chem. C* **2012**, *116*, 9114–9121.

(47) Di Valentin, C.; Selloni, A. Bulk and surface polarons in photoexcited anatase TiO<sub>2</sub>. *J. Phys. Chem. Lett.* **2011**, *2*, 2223–2228.

(48) Cheng, J.; VandeVondele, J.; Sprik, M. Identifying trapped electronic holes at the aqueous TiO<sub>2</sub> interface. *J. Phys. Chem. C* **2014**, *118*, 5437–5444.

(49) Wallace, S. K.; McKenna, K. P. Facet-dependent electron trapping in TiO<sub>2</sub> nanocrystals. *J. Phys. Chem. C* **2015**, *119*, 1913–1920.

(50) McKenna, K. P.; Wolf, M. J.; Shluger, A. L.; Lany, S.; Zunger, A. Two-dimensional polaronic behavior in the binary oxides m–HfO<sub>2</sub> and m–ZrO<sub>2</sub>. *Phys. Rev. Lett.* **2012**, *108*, No. 116403.

(51) Nolan, M. First-principles prediction of new photocatalyst materials with visible-light absorption and improved charge separation: Surface modification of rutile TiO<sub>2</sub> with nanoclusters of MgO and Ga<sub>2</sub>O<sub>3</sub>. *ACS Appl. Mater. Interfaces* **2012**, *4*, 5863–5871.

(52) Iwaszuk, A.; Lucid, A. K.; Razeed, K. M.; Nolan, M. First principles investigation of anion-controlled red shift in light absorption in ZnX (X = O, S, Se) nanocluster modified rutile TiO<sub>2</sub>. *J. Mater. Chem. A* **2014**, *2*, 18796–18805.

(53) Iwaszuk, A.; Nolan, M. Reactivity of sub 1 nm supported clusters: (TiO<sub>2</sub>)<sub>n</sub> clusters supported on rutile TiO<sub>2</sub> (110). *Phys. Chem. Chem. Phys.* **2011**, *13*, 4963–4973.



- (54) Fronzi, M.; Daly, W.; Nolan, M. Reactivity of metal oxide nanocluster modified rutile and anatase  $\text{TiO}_2$ : oxygen vacancy formation and  $\text{CO}_2$  interaction. *Appl. Catal., A* **2016**, *521*, 240–249.
- (55) Iwaszuk, A.; Mulheran, P. A.; Nolan, M.  $\text{TiO}_2$  nanocluster modified-rutile  $\text{TiO}_2$  photocatalyst: a first principles investigation. *J. Mater. Chem. A* **2013**, *1*, 2515–2525.
- (56) Nolan, M. Electronic coupling in iron oxide-modified  $\text{TiO}_2$  leads to a reduced band gap and charge separation for visible light active photocatalysis. *Phys. Chem. Chem. Phys.* **2011**, *13*, 18194–18199.
- (57) Morgan, B. J.; Watson, G. W. A density functional theory + U study of oxygen vacancy formation at the (110), (100), (101), and (001) Surfaces of Rutile  $\text{TiO}_2$ . *J. Phys. Chem. C* **2009**, *113*, 7322–7328.
- (58) Di Valentin, C.; Pacchioni, G.; Selloni, A. Reduced and n-type doped  $\text{TiO}_2$ : nature of  $\text{Ti}^{3+}$  species. *J. Phys. Chem. C* **2009**, *113*, 20543–20552.
- (59) Ji, Y.; Wang, B.; Luo, Y. Location of trapped hole on rutile- $\text{TiO}_2$ (110) surface and its role in water oxidation. *J. Phys. Chem. C* **2012**, *116*, 7863–7866.
- (60) Carey, J. J.; Legesse, M.; Nolan, M. Low valence cation doping of bulk  $\text{Cr}_2\text{O}_3$ : charge compensation and oxygen vacancy formation. *J. Phys. Chem. C* **2016**, *120*, 19160–19174.
- (61) Deskins, N. A.; Rousseau, R.; Dupuis, M. Distribution of  $\text{Ti}^{3+}$  surface sites in reduced  $\text{TiO}_2$ . *J. Phys. Chem. C* **2011**, *115*, 7562–7572.
- (62) Chrétien, S.; Metiu, H. Electronic structure of partially reduced rutile  $\text{TiO}_2$  (110) surface: where are the unpaired electrons located? *J. Phys. Chem. C* **2011**, *115*, 4696–4705.
- (63) Karwacki, C. J.; Ganesh, P.; Kent, P. R. C.; Gordon, W. O.; Peterson, G. W.; Niu, J. J.; Gogotsi, Y. Structure–activity relationship of Au/ $\text{ZrO}_2$  catalyst on formation of hydroxyl groups and its influence on CO oxidation. *J. Mater. Chem. A* **2013**, *1*, 6051–6062.
- (64) Ganesh, P.; Kent, P. R. C.; Veith, G. M. Role of hydroxyl groups on the stability and catalytic activity of Au clusters on a rutile surface. *J. Phys. Chem. Lett.* **2011**, *2*, 2918–2924.
- (65) Kresse, G.; Furthmüller, J. Efficiency of ab-initio total energy calculations for metals and semiconductors using a plane-wave basis set. *Comput. Mater. Sci.* **1996**, *6*, 15–50.
- (66) Kresse, G.; Furthmüller, J. Effective iterative schemes for *ab initio* total energy calculations using a plane wave basis set. *Phys. Rev. B* **1996**, *54*, 11169–11186.
- (67) Perdew, J. P.; Chevary, J. A.; Vosko, S. H.; Jackson, K. A.; Pederson, M. R.; Singh, D. J.; Fiolhais, C. Atoms, molecules, solids, and surfaces: applications of the generalized gradient approximation for exchange and correlation. *Phys. Rev. B* **1992**, *46*, 6671–6687.
- (68) Blöchl, P. E. Projector augmented wave method. *Phys. Rev. B* **1994**, *50*, 17953–17979.
- (69) Nolan, M.; Watson, G. W. Hole localization in Al doped silica: a DFT + U description. *J. Chem. Phys.* **2006**, *125*, No. 144701.